UNSIVERSITY OF THESSALY
SCHOOL OF ENGINEERING
DEPARTMENT OF MECHANICAL ENGINEERING

Diploma thesis

Carbon monoxide (CO) tolerance estimation of anode catalysts (Pt_xIr_y/C & Pt_xPd_y/C) for proton exchange polymer membrane fuel cells (PEMFCs)

by

Koukoura Konstantino-Ioanni
Balkourani-Tsiatsiani Georgia

SUPERVISOR
Prof. Tsiakaras Panagiotis

Submitted in fulfillment of the requirements for the Diploma in the Department of Mechanical Engineering of the University of Thessaly

Volos, 2020

ΠΑΝΕΠΙΣΤΗΜΙΟ ΘΕΣΣΑΛΙΑΣ
ΠΟΛΥΤΕΧΝΙΚΗ ΣΧΟΛΗ
ΤΜΗΜΑ ΜΗΧΑΝΟΛΟΓΩΝ ΜΗΧΑΝΙΚΩΝ

Διπλωματική εργασία

Εκτίμηση της ανοχής στο μονοξείδιο του άνθρακα (CO), ανοδικών καταλυτών (Pt_xIr_y/C & Pt_xPd_y/C) για κυψελίδες καυσίμου πολυμερικής μεμβράνης πρωτονιακής αγωγιμότητας (PEMFCs)

υπό

Κούκουρα Κωνσταντίνο-Ιωάννη
Μπαλκουράνη-Τσιατσιάνη Γεωργία

Επιβλέπων
Καθηγητής Τσιακάρας Παναγιώτης

Υπεβλήθη για την εκπλήρωση μέρους των απαιτήσεων για την απόκτηση του
Διπλώματος Μηχανολόγου Μηχανικού
Βόλος, 2020

© Κούκουρας Κωνσταντίνος & Μπαλκουράνη-Τσιατσιάνη Γεωργία

Η έγκριση της διπλωματικής εργασίας από το Τμήμα Μηχανολόγων Μηχανικών της Πολυτεχνικής Σχολής του Πανεπιστημίου Θεσσαλίας δεν υποδηλώνει αποδοχή των απόψεων του συγγραφέα (Ν. 5343/32 αρ. 202 παρ. 2).

Εγκρίθηκε από τα Μέλη της Τριμελούς Εξεταστικής Επιτροπής:

1st Examiner: Dr Tsiakaras Panagiotis (Supervisor)
Professor of Department of Mechanical Engineering,
School of Engineering
University of Thessaly

2nd Examiner: Dr Charalampous Georgios
Assistant Professor of Mechanical Engineering,
School of Engineering
University of Thessaly

3rd Examiner: Dr Angeliki Brouzgou
Senior Researcher and Teaching Staff of Department of Mechanical Engineering,
School of Engineering
University of Thessaly

ACKNOWLEDGEMENTS

The first person we would like to express our gratitude, is our professor, Dr. Tsiakaras Panagiotis, for his exemplary work as a supervisor and as a mentor. His knowledge, interest, experience, consultation and endless support and encouragement towards us, were some of the tools that helped us through this part of our postgraduate experience. Also, he granting us access at the Laboratory of Alternative Energy Conversion Systems at the Department of Mechanical Engineering in University of Thessaly was a great help for accomplishing our experimental work as well as getting to know the procedures taking place in a real scientific lab. In addition, we want to express our regards to our co-supervisor Dr. Angeliki Brouzgou and the committee member Dr. Charalampous Georgios.

The lab personnel also deserve a great part of our acknowledgment Dr. Antonios Seretis and Dr. Sotiria Kontou, which did not only do a splendid work guiding, assisting and supporting us, but they considered us as a part of the lab and colleagues, making this procedure worth-while and educative for our future steps.

We would like to thankfully express our gratitude to our parents (Konstantinos Koukouras to his mother Dimitra and his father George and Georgia Balkourani to her mother Areti and her father Ioannis) for the love, the moral and financial support provided, not only during elaborating the present thesis, but also throughout our studies at the Department of Mechanical Engineering in University of Thessaly. Last but not least, we would like to thank our friends for their love and support (Elli, Linta, Vasilis, Afroditi, Olga).

ABSTRACT

With the exhaustion of conventional fuels and the continuing increase in energy demands of today's society the shift to clean energy technologies, for the storage and the conversion of energy, is necessary.

The most feasible, sustainable and environmentally friendly of these clean technologies is consider the electrochemical energy storage and conversion. Among these technologies are fuel cells, batteries, electrochemical supercapacitors, hydrogen generation-storage and energy that comes from the forces of nature (wind, sun etc.). Some of them are already in use and others have recently begun to apply with slow but steady progress in important application areas such as transportation. Thus, the need to overcome the obstacles that lay in the application areas is necessary. Power densities, energy densities, cost and durability are the obstacles for the wide use of these electrochemical devices. In this work will be examined the carbon monoxide tolerance of anode catalyst (Pt_xIr_y/C and Pt_xPd_y/C) of low temperature proton exchange polymer membrane fuel cells (PEMFCs).

In the first section of this work general information are provided about the renewable energy sources and the electrochemical devises for storage and conversion of energy. Then a detailed description about the operation and the reactions taking place inside the PEMFCs is provided with focus on the hydrogen oxidation reaction and its obstruction by the poisoning of the anode catalysts due to the small amount of carbon monoxide contained in the fuel supply. In the experimental part are presented two series of w.t. 20% catalyst, supported on carbon Vulcan XC72 (Pt_xPd_y, Pt_xIr_y, atomic ratios 3:1, 1:1 and 1:3), for the examination of the reaction of hydrogen oxidation and the tolerance of the catalyst in presence of 400 ppm CO. For the determination of which in the most tolerant in presence of CO, a series of electrochemical test (Cyclic voltammetry, electrochemical impedance spectroscopy, linear sweep voltammetry and chronoamperometry) was conducted.

ΠΕΡΙΛΗΨΗ

Με την υπεράντληση των ορυκτών καυσίμων, την συνεπαγόμενη ζημία που αυτή επιφέρει στο περιβάλλον και τη συνεχόμενη αύξηση των ενεργειακών αναγκών της σημερινής κοινωνίας καθίσταται αναγκαία η μετάβαση σε τεχνολογίες καθαρής ενέργειας, για την αποθήκευση και μετατροπή της ενέργειας. Από τις πιο εφικτές, βιώσιμες και φιλικές προς το περιβάλλον ¨καθαρές¨ τεχνολογίες είναι αυτές της αποθήκευσης και της μετατροπής της ηλεκτροχημικής ενέργειας. Μεταξύ αυτών των τεχνολογιών είναι οι κυψέλες καυσίμου, οι μπαταρίες, οι ηλεκτροχημικοί υπερπυκνωτές, η παραγωγή-αποθήκευση υδρογόνου και η ενέργεια που προέρχεται από τις δυνάμεις της φύσης (άνεμος, ήλιος κ.λ.π.). Ορισμένες από αυτές χρησιμοποιούνται ήδη και άλλες έχουν αρχίσει να εφαρμόζουν πρόσφατα με αργή αλλά σταθερή πρόοδο σε σημαντικούς τομείς εφαρμογής όπως οι μεταφορές. Έτσι είναι απαραίτητη η ανάγκη να ξεπεραστούν τα εμπόδια που υπάρχουν στις περιοχές εφαρμογής. Η πυκνότητα ισχύος, η πυκνότητα ενέργειας, το κόστος και η ανθεκτικότητα αποτελούν εμπόδια για την ευρεία χρήση αυτών των ηλεκτροχημικών συσκευών. Σε αυτή την εργασία θα εξεταστεί η ανοχή, στην παρουσία μονοξειδίου του άνθρακα, καταλυτών ανόδου (Pt_xIr_y/C and Pt_xPd_y/C) κυψελών καυσίμου ανταλλαγής πρωτονίων πολυμερικής μεμβράνης χαμηλών θερμοκρασιών (PEMFCs).

Στην πρώτη ενότητα αυτής της εργασίας παρέχονται γενικές πληροφορίες σχετικά με τις ανανεώσιμες πηγές ενέργειας και τις ηλεκτροχημικές συσκευές αποθήκευσης και μετατροπής της ενέργειας. Στη συνέχεια, παρέχεται μια λεπτομερής περιγραφή της λειτουργίας και των αντιδράσεων που λαμβάνουν χώρα εντός των PEMFC με έμφαση στην αντίδραση οξείδωσης υδρογόνου και την παρεμπόδιση της από τη δηλητηρίαση των καταλυτών ανόδου λόγω της μικρής ποσότητας μονοξειδίου του άνθρακα που περιέχεται στην παροχή καυσίμου. Στο πειραματικό μέρος παρουσιάζονται δύο σειρές 20% κ.β. καταλύτη, υποστηριζόμενες σε άνθρακα Vulcan XC72 (Pt_xPd_y, Pt_xIr_y, ατομικές αναλογίες 3: 1, 1: 1 και 1: 3), για την εξέταση της αντίδρασης οξείδωσης υδρογόνου και της ανοχής των καταλυτών στην παρουσία

400 ppm CO. Για τον προσδιορισμό του πιο ανεκτικού στην παρουσία CO, διεξήχθη μια σειρά ηλεκτροχημικών δοκιμών (κυκλική βολταμετρία, φασματοσκοπία ηλεκτροχημικής εμπέδησης, γραμμική βαλταμετρία σάρωσης περιστρεφόμενου δίσκου και χρονοαμπερομετρία).

Contents

ACKNOWLEDGEMENTS……………………………………………..**i**
ABSTRACT………………………………………………………...**ii**
ii
LIST OF FIGURES………………………………………………..**viii**
LIST OF TABLES…………………………………………………**xii**
1 Introduction………………………………………………………**1**
1.1 Renewable energy sources... 2
1.1.1 Solar energy.. 3
1.1.2 Wind energy 3
1.1.3 Biomass energy 4
1.1.4 Hydropower energy and Marine energy.............................. 4
1.1.5 Geothermal energy 5
1.1.6 Hydrogen as fuel... 6
1.2 Electrochemical devices for energy storage and conversion.... 8
1.2.1 Batteries.. 8
1.2.2 Super-capacitors 10
1.2.3 Photovoltaic cells.. 11
1.2.4 Fuel cells... 12
2 PEMFC 15
2.1 General information and commercialization of PEMFCs 15
2.2 Working principles of PEMFC-H_2 16
2.3 Why pure Pt is used as a catalyst... 18
2.4 Hydrogen fuel and impurities 19
2.5 Catalysts and CO-poisoning 20
2.6 Poisoning mechanisms... 21
3 Theory of experimental techniques 23
3.1 Physicochemical characterization.. 23
3.1.1 X-Ray diffraction (XRD) 23
3.1.2 Transmission Electron Microscopy (TEM)....................... 24

3.1.3 Scanning electron microscopy (SEM) 25
3.2 Electrochemical characterization 26
3.2.1 Rotating disk electrode technique (RDE) 26
3.2.2 Cyclic Voltammetry (CV) 27
3.2.3 Chronoamperometry (CA) 29
3.2.4 Linear Sweep Voltammetry (LSV) 30
3.2.5 Electrochemical Impedance Spectroscopy (EIS) 31
4 Experimental part 33
4.1 Catalytic ink preparation 33
4.2 Electrochemical characterization 33
4.3 Experimental procedures 34
4.3.1 Cyclic voltammetry 34
4.3.2 Linear sweep voltammetry with rotating disk electrode ... 35
4.3.3 Chronoamperometry 35
4.3.4 Electrochemical Impedance Spectroscopy 35
4.3.5 Test of durability to CO in HOR 35
5 Experimental results 39
5.1 Physiochemical characterization 39
5.2 Electrochemical characterization 42
5.2.1 Catalyst activation 42
5.2.2 Electrochemical active surface area (ECSA) 43
5.3 Linear sweep voltammetry results 46
5.3.1 Linear sweep voltammetry results for different flow rates of H_2/N_2 46
5.3.2 Investigation of electrocatalyst tolerance in the presence of carbon monoxide 54

6 Concluding remarks……………………………………………**63**
7 References…………………………………………………..**70**

-

LIST OF FIGURES

Figure 1-1 The pie chart depicting the share of renewable energy on the total energy produced globally. The share of individual renewable sources is highlighted (data obtained from the clean energy trend report of IEA) [2]. 2

Figure 1-2 The share of modern renewables, out of all renewables increased dramatically from 3.1% in 1990 to 35.7% in 2018 [2]....................... 2

Figure 1-3 Schematic of hydroelectric power plant [4]. 5

Figure 1-4 Schematic of primary battery [6]... 9

Figure 1-5 Schematic of charge/discharge cycle of a typical super-capacitor[9]. 10

Figure 2-1 A schematic of a proton exchange membrane fuel cell [16]. 18

Figure 2-2 Pt has the highest activity of all bulk metals for hydrogen bonding energy[14]. 19

Figure 3-1 Reflected X-rays by atoms in a lattice plane interface constrictively in direction given by Bragg's Law (left) [19], XRD patterns of different catalyst (right) [20]. 24

Figure 3-2 Transmission electron microscope and its components (left) [22], Series of typical phase-contrast TEM images of unsupported Au nanoparticles (right) [23]. 25

Figure 3-3 Working principles of SEM (left) [24], Examples of scanning electron micrographs (right) [25].. 25

Figure 3-4 Streamlines for flow and vector representation of fluid velocities near the surface of a rotating disc electrode [27]. 27

Figure 3-5 (a) The potential vs. time waveform and (b) a typical cyclic voltammogram of a oxidation- reduction process [30]. 29

Figure 3-6 Single step chronoamperometry a) excitation waveform b) response waveform [31]. 30

Figure 3-7 A typical voltammogram potential vs. time [33]...............31

Figure 3-8 Impedance Z phase shift Φ, Z' the real part, Z'' the imaginary part of the impedance in the complex plane [34]. 32

Figure 5-1 Transmission electron microscopy micrographs of: (a) Pd/C, (b)Pt_1Pd_3/C, (c) Pt_3Pd_1/C, (d) Pt_1Pd_1/C...39

Figure 5-2 Transmission electron microscopy micrographs of: (a) Ir/C, (b) Pt/C, (c) Pt_1Ir_1/C, (d) Pt_1Ir_3/C, (e) Pt_3Ir_1/C. 40

Figure 5-3 XRD analysis results, (a) Pt_xIr_y/C and (b) Pt_xPd_y/C. 41

Figure 5-4 XPS and EDX analysis results. 41

Figure 5-5 Activation-purification of the deposited catalysts. 43

Figure 5-6 Cyclic voltammetry curve of 20 wt.% (a) Pt_xIr_y/C and (b) Pt_xPd_y/C for the hydrogen oxidation reaction, in a N_2 saturated 0,1 M $HCLO_4$ solution at a scanning rate of 50 mV s^{-1} , from 0.1V to 1.2V (vs. RHE), measurements were taken at 30° C . The marked areas are used for the calculation of the ECSA. 45

Figure 5-7 LSV curves in H2-saturated 0.1 M HClO4 aqueous solution, at rotation rates 400, 1000, 1600, 2200, 2800 rpm, at a scan rate of 5 mV s-1 for (a) Pt/C, (b)Pd/C, (c) Pt3Pd/C and (d) PtPd/C, (e) PtPd3/C2 before exposure to CO. 47

Figure 5-8 LSV curves in H2-saturated 0.1 M HClO4 aqueous solution, at rotation rates 400, 1000, 1600, 2200, 2800 rpm, at a scan rate of 5 mV s-1 for (a) Pt/C, (b) Ir/C, (c) Pt3Ir/C, (d) PtIr/C, (e) PtIr3/C before exposure to CO. 48

Figure 5-9 LSV curves in H2-N2 10/40 (cc/min) 0.1 M HClO4 aqueous solution, at rotation rates 400, 1000, 1600, 2200 rpm, at a scan rate of 5 mV s-1 for (a) Pt/C, (b)Pd/C, (c) Pt3Pd/C and (d) PtPd/C, (e) PtPd3/C. 49

Figure 5-10 LSV curves in H_2/N_2 (10/40 cc/min) 0.1 M $HClO_4$ aqueous solution, at rotation rates 400, 1000, 1600, 2200 rpm, at a scan rate of 5 mV s^{-1} for (a) Pt/C, (b) Ir/C, (c) Pt_3Ir/C, (d) PtIr/C, (e) $PtIr_3$/C. 50

Figure 5-11 Tafel plots in H2-saturated 0.1 M HClO4 aqueous solution, at rotation rate 1600 rpm, at a scan rate of 5 mV s-1 for (a) PtxPdy/C, (b) PtxIry/C before exposure to CO. 52

Figure 5-12 Tafel plots curves in H2/N2 (10/40 cc/min) 0.1 M HClO4 aqueous solution, at rotation rate 1600 rpm, at a scan rate of 5 mV s-1 for (a) PtxPdy/C, (b) PtxIry/C before exposure to CO. 53

Figure 5-13 Chronoamperometry results: curves of (a) Pt_xPd_y/C duration 3 hours, (b) Pt_xIr_y/C duration 3 hours, (c) Pt_xPd_y/C duration 6 hours, (d) Pt_xIr_y/C duration 6 hours, (e) Pt_xPd_y/C duration 9 hours, (f) Ir/C, Pt/C and Pd/C electrocatalyst for the durations 1, 2, 3 hours respectively in H_2/CO 10/40 (cc/min) 0.1 M $HCLO_4$ aqueous solution at 1600 rpm, at -0,2V potential step. 55

Figure 5-14 Electrooxidation of adsorbed CO in 0.1M $HClO_4$, 50 mV s^{-1}.. 57

Figure 5-15 Electrooxidation of adsorbed carbon monoxide in 0.1M $HClO_4$, 50mV s^{-1}. 58

Figure 5-16 Percentage coverage of active centers with CO, as a function of exposure time at 400 ppm CO (a), percentage of coverage of active centers by CO as a function of Pt / Pd ratio (b). 59

Figure 5-17 Electrooxidation peaks of CO for Pt_xIr_x/C catalysts......... 59

Figure 5-18 Percentage coverage of active centers with CO, as a function of exposure time at 400 ppm CO for Pt_xIr_y/C group of electrocatalysts. 60

Figure 5-19 Linear scan curves in H2-saturated 0.1M $HClO_4$, 1600 rpm, before exposure to CO and after exposure for 3,6 and 9 hours (top line) and Tafel curves for the corresponding linear scan curves. 61

Figure 6-1 Transmission electron microscopy images (TEM) of (a) PtRu/C and (b) $PtRu_3$/C, (c) CO-stripping curves and (d) particle diameters and ECSAs of PtRu/C and $PtRu_3$/C [41].. 64

Figure 6-2 Tafel plots in H_2-saturated 0.1 M $HClO_4$ aqueous solution, at rotation rate 1600 rpm, at a scan rate of 5 mV s^{-1} for (a) Pt_xPd_y/C, (b) Pt_xIr_y/C before exposure to CO. 65

Figure 6-3 (a)Pt_xPd_y/C, (b) Pt_xIr_y/C maximum hours of chronoamperometry in H_2/CO 10/40 (cc/min) 0.1 M $HCLO_4$ aqueous solution at 1600 rpm, at -0,2V potential step. Percentage coverage of active centers with CO, as a function of exposure time at 400 ppm CO for (c) Pt_xPd_y/C and (d)Pt_xIr_y/C... 66

Figure 6-4 LSV curves (a, c, e, g) and the corresponding Tafel plots(b, d, f, h) in H_2-saturated 0.1 M $HClO_4$ aqueous solution, at 1600 rpm, at a scan rate of 5 mV s^{-1} for Pt_xPd_y/C catalysts before and after exposure to CO for different time intervals. 68

LIST OF TABLES

Table 1: Electrochemical active surface area for Pt_xIr_y and Pt_xPd_y catalysts. 46

Table 2: Kinetic current I_k when low, medium, and high potential prices are applied for catalysts Pt_xPd_y/C. Prices collected from LSV curves in H_2-saturated, 0.1 M $HCLO_4$ aqueous solution, at rotation rate of 1600 rpm, and scan rate of 5 mV s^{-1}. 51

Table 3: Kinetic current I_k when low, medium, and high potential prices are applied for catalysts Pt_xIr_y/C. Prices collected from LSV curves in H_2-saturated, 0.1 M $HCLO_4$ aqueous solution, at rotation rate of 1600 rpm, and scan rate of 5mVs-1. 52

Table 4: CO electrooxidation information. 58

Table 5: Main peak potentials ($E_{main\ peak}$) and relative ratios of catalyst sites poisoned by CO for a series of Pt_xPd_y catalysts tested at 25^o C [45]. 63

CHAPTER I

1 Introduction

Energy demand across the world is constantly increasing. That increase is firstly caused from the economic development and the improvements in the quality of people’s life. Secondly is due to the world’s population raise and finally from the rapid industrialization of the developing nations. The most powerful economies have built their progress on conventional (mineral) energy sources like oil, coal, and natural gas. Burning fossil fuels for industrial needs and human activities (electricity, heat and transportation) brought a large growth of the greenhouse gasses emissions (CO_2 & H_2O), causing significant adverse impacts on the environment, the global climate change, and on human’s health and their quality of life. In growing greenhouse gasses emissions (EDGAR, European Commission and Netherlands Environmental Assessment Agency, 2018) leading role has China with United States in the second place, followed by India and Russia in the third and fourth place, respectively [1].

Taking the above into account, our society is slowly looking for more sustainable solutions of producing and consuming energy. Less wastes, reduced air pollution, conservation and increase of native forests, and reduction of greenhouse gasses emissions are some of the main targets. Ever since environmental protection is a priority of the humanity, renewable energy sources and clean fuel technologies are investigated. Renewable energy is collected from renewable resources, which are naturally refueled on a human timescale. For example, energy that comes from sunlight, wind, rain, waves, tides, biomass and geothermal heat. Renewable energy conversion systems are rapidly becoming more efficient and cheaper, and they also have the potential of providing energy services with zero or almost zero emissions.

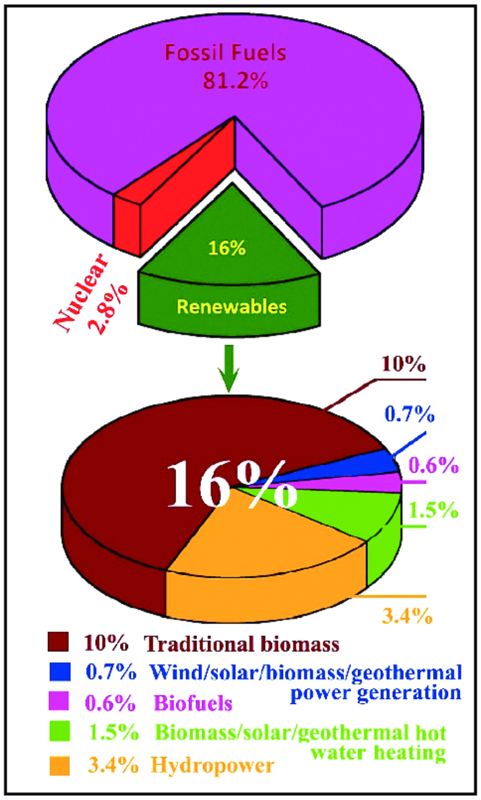

Figure 1-1 The pie chart depicting the share of renewable energy on the total energy produced globally. The share of individual renewable sources is highlighted [2].

1.1 Renewable energy sources

Solid biofuels and hydroelectric power influenced much of renewables growth between 1990 and 2000 as shown on Figure 1-2.

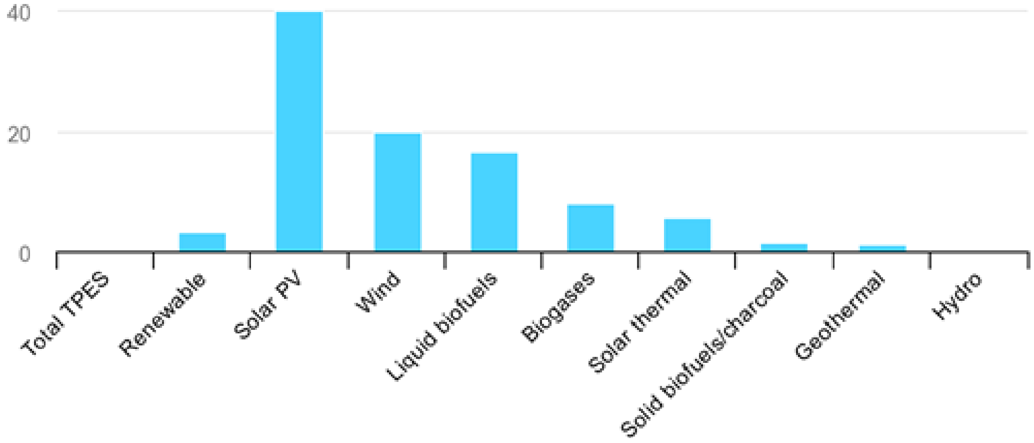

Figure 1-2 The share of modern renewables, out of all renewables increased dramatically from 3.1% in 1990 to 35.7% in 2018 [2].

Nevertheless, the renewable energy sources still contribute the minimum to the total energy supply. As we can see on Figure 1-1, the sum of renewables (biomass, hydropower, solar power, geothermal power and wind power) amounts only to 16% of total energy supply. Despite this, in OECD countries (Organization for Economic Co-operation and Development) the share of modern renewables out of all renewables presents a dramatic increase from 3.1% in 1990 to 35.7% in 2018.

1.1.1 Solar energy

Solar thermal energy is abundant and can be used in both direct and indirect forms. The sun emits a huge amount of energy up to 3.8 × 1023 kW, 1.8 × 1014 kW out of which is absorbed on the earth. There is a large amount available solar energy that can be used to:

i) solar photovoltaic cell that directly convert light-energy to electricity, either

ii) systems that use specific surfaces to concentrate the solar radiation power into a small beam. The concentrated power causing electricity production by converting to heat.

iii) solar thermal heating and cooling technologies, by collecting the sunlight and using the heat for spaces heating and cooling, for hot water supply and pool heating for industrial applications, residential and commercial usage.

These technologies have numerous systems installed around the world because they are technically well proven and over the last decades their cost has fallen [1, 3].

1.1.2 Wind energy

Wind power is produced by converting the available wind energy to a useful form such as electricity or mechanical power through the use of wind turbines. Wind energy is a commonly used, competitive, pollution-free technology for electricity production today. At a wind turbine, as wind flows through the aerodynamically designed blades, the motion energy is converted into rotating mechanical power that used to drive a generator. The power produced from these technologies could reduce by several units the emissions of greenhouse gasses and other [1, 3].

1.1.3 Biomass energy

Biomass energy is the form of renewable energy that comes from the conversion of biomass into a form of energy that can be easily used such as heat, electricity and biofuels. Biomass is called every organic material comes from plants, trees and fields that storage sun's energy through photosynthesis. Biomass is collected either directly from the land as agricultural waste products or as organic waste (households - food industry).

Biomass has a lot in common with fossil fuels. It can be burned to give energy or can be used as feedstock to produce various liquid or gas fuels. Biofuels can be transported and stored giving us the opportunity to produce electricity or heat when needed. These characteristics make biomass energy very competitive and promising for the future.

The conversion of feedstock to biomass energy can be done via bio-chemical and thermo-chemical processes such as gasification, combustion, pyrolysis and anaerobic digestion.

Nevertheless, there are significant barriers in bioenergy production. The biofuels have low energy densities in comparison with fossil fuels, and it follows that we need bigger quantities to produce the same amount of energy. That is the reason why the cost of collection and transportation can be high. Also, biomass quantity depends on various unstable factors like agriculture productivity, and the cycle of the water through the year so there is an opportunity cost [1, 3].

1.1.4 Hydropower energy and Marine energy

Hydropower is the power produced by the motion of water in the hydrological cycle, which is caused by solar radiation. The most common form is dams, and follow harnessing wave and tidal power. We use the flow of water in rivers that is driven by the gravity from higher to lower heights, to generate hydropower. The flowing water gives energy that can be converted to electricity through turbines.

Marine or ocean energy comes from waves, ocean currents, tidal range, ocean thermal energy conversion and tidal currents. For each form of them a different technology is required, in order to be converted into a useful form of energy. The ocean energy is not very common and most of the sectors included are still in progress, however many developments are going to happen to increase the amount of ocean energy produced and used to fulfill human energy needs [1, 3].

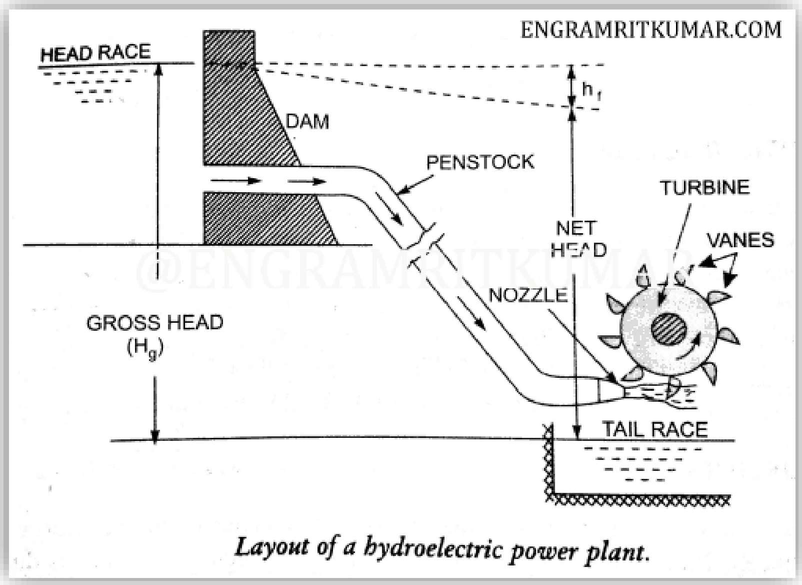
ENGRAMRITKUMAR.COM
HEAD RACE
DAM
h_f
PENSTOCK
TURBINE
NET HEAD
VANES
@ENGRAMRITKUMAR
NOZZLE
GROSS HEAD (H_g)
TAIL RACE
Layout of a hydroelectric power plant.

Figure 1-3 Schematic of hydroelectric power plant [4].

1.1.5 Geothermal energy

Geothermal energy is extracted from the ground by natural processes and it is a form of renewable energy. This can be used either for a small energy demand, by providing heat for a residential unit through a geothermal heat pump (GHP), or for bigger energy needs by providing energy through a geothermal powerplant.

The geothermal systems provide heat that vary in temperature depending on the depth. Hydrothermal systems with temperature greater than 180°C are associated with recent volcanic areas. Hydrothermal systems with temperatures between 180-100°C and lower (less than 100°C) are associated with continental regions where above regular heat production there is also the radioactive isotopes decay that increases the heat flow on the ground.

Geothermal energy sources are separated to hydrothermal systems, conductive systems and deep aquifers. All of them consist of thermal energy, from various depths, that is trapped into rocks, steam or liquid water. Geothermal energy sources are also classified by utilization: 1) to generate electric power, 2)to use directly for heat, or 3) to be combined for heat and power - in cogeneration applications. The most commercially exploited and known geothermal system is the geothermal heat pump (GHP) [3].

1.1.6 Hydrogen as fuel

Hydrogen is not an energy source itself, but it can be produced from other sources of energy. It can be produced by fossil fuels or nuclear power, but it can also be produced by renewable sources by different conversion processes. The energy content of hydrogen is 33.3 $kWhkg^{-1}$ (lower heating value, LHV), and 39.4 $kWhkg^{-1}$ (upper heating value, UHV). The first car with an internal combustion engine, invented by Francoise Isaac de Rivaz in 1807 and used a mixture of hydrogen and oxygen as a fuel. In the 20th century hydrogen starts to be used from nuclear submarines, airships, and launching systems from the 1960s. Later hydrogen becomes a fuel of choice for rockets and launchers [1].

Fuel cells progress has contributed to hydrogen's applications, mainly in the transportation sector. Cars based on fuel cells with polymer electrolyte membrane (PEMFCs) are being demonstrated world-wide. Its usage provides some important advantages such as high efficiency in well-to-wheel assessment, silent mode operation and energy-efficient drive train. Hydrogen has much greater energy content per unit weight than other fuels like methanol, ethanol, petrol, diesel or kerosene, but it can be hazardous to handle due to its high flammability range. Flammability limits of hydrogen increase with temperature. Hydrogen-fueled cars, are said to be about 1.5-2.5 times more efficient than gasoline-advanced cars on a tank-to-wheels basis and they are pollutant-free. For the development of a future hydrogen economy, an efficient and secure way of storing hydrogen in a variety of applications, mobile, stationary and portable, is required. Some ways of hydrogen storage include liquid cryogenic hydrogen (LH_2), compressed hydrogen gas (CGH_2) and solid-state hydrogen storage (SSH_2). Onboard hydrogen storage is one of the most important barriers we must overcome for entering the commercialization phase of hydrogen-fueled light vehicles. Using hydrogen in the transport sector will also help reducing greenhouse gasses emissions -such as CO, NO_x, volatile organic components (VOCs) and particulate matter (PM-solid or liquid particles found in the air)- by more than 70% for NO_x and other pollutants.

The major amount of hydrogen used, is produced with different technologies from fossil fuels, from biomass or from water.

1) From fossil fuels hydrogen is produced by thermal cracking of natural gas, steam reforming of natural gas, partial oxidation (POX) of heavy fraction or coal gasification.
2) From biomass by burning, fermenting, pyrolysis, or biological production.
3) From water hydrogen is taken by electrolysis, gasification followed by liquefaction, photolysis, thermo-chemical processes, thermolysis and combination of biological, thermal and electrolytic processes.

Some of the main ways of hydrogen isolation/production are explained below.

Reforming processes, are the methods of preference for massive hydrogen production today. Some of the main reforming processes are POX, steam reforming, and autothermal reforming. Typically, the feedstock used is natural gas, but also hydrocarbons in liquid form can be used. Steam reforming of natural gas is currently the cheapest way of producing hydrogen and is mainly used at petrochemical and chemical industries.

Electrolytic hydrogen costs are not being able to compete with the production costs for hydrogen by conventional steam reforming of natural gas or other fossil fuels. That leads to an increasing interest with regard to PEM - electrolysis technology. The efficiency of PEM - electrolysis could reach a level of 55% - 70%. PEM water electrolysis is still rather expensive due to the use of platinum-based family catalysts that increasing the cost and the sensitivity of the proton exchange membrane. Nevertheless, PEM - electrolysis is well suited to be coupled with wind and solar energy.

Gasification systems can utilize coal, petroleum coke, biomass and municipal and hazardous wastes. There are three main steps:

4) conversion of coal feedstock, in the presence oxygen or air and steam (or another oxidant), to syngas at high temperatures of 1000-1500 °C in a gasification reactor
5) catalytic shift reaction
6) and purification of the produced hydrogen, typically from residual carbon and ash.

Depending on the production technology, in the syngas could be presented some water, CO_2 and CH_4 including traces of components such as hydrogen cyanide (HCN), hydrogen chloride gas (HCl), hydrogen sulphide (H_2S) and carbonyl sulphide (COS). Generated syngas can either be used directly to produce electricity or be farther processed to pure hydrogen to be used for hydrocracking of petroleum or ammonia production. During the pyrolytic process the biomass is heated at 370-550°C at 0.1-0.5 MPa in the absence of air to convert it into liquid oils, solid charcoal and gaseous compounds. Biomass that can pyrolytically processed can be, for example, pelletized peanut shells, post-consumer residues (plastics), mixed biomass and synthetic polymers as well as bagasse, switchgrass and a nutshell mixture composed of 40% almond nutshells, 40% almond pruning and 20% walnut shells.

Hydrogen is produced also by splitting water. That can be done with three main processes: electrolysis, photochemical processes and thermodynamic cycles [5].

1.2 Electrochemical devices for energy storage and conversion

The knowledge and the chance of using power that derives from renewable energy sources requires the availability of effective devices that give us the ability to convert the energy in a usable form and store the amount of energy produced for future use.

The modern electrochemistry faces two great challenges.

- First, the challenge of developing rechargeable batteries for load-leveling applications that will be able to cycling huge amounts of electrical energy comes from renewable sources such as wind and sun.
- Second, the development of applications that provide energy density. In this section the ultimate solution may be hydrogen-based fuel cells, such as in electric vehicles where high specific energy density is crucial.

Also, for some applications super-capacitors (due to their high-power density) in combination with batteries are used. When that happens, the rechargeable batterie works as the energy supplier and the super-capacity provides high power.

1.2.1 Batteries

In this section, we mention only the main, most known and widely used battery systems. However, the progress in battery – technologies provide a much larger field, than that we describe. Generally, batteries use the energy comes from an exothermal redox reaction of the following general type:

$$A + B \leftrightarrow C + D, \text{ where } \Delta H << 0 \tag{1.1}$$

The tow reactions that take place, reduction and oxidation, are separated by an ionically conducting medium and the electrons flow from the reductant (working as the anode material) to the oxidant (working as the cathode side) producing electrical work.

The anode reaction can be described as:

$$B \rightarrow C + ne^- \qquad (1.2)$$

whereas the cathode reaction is:

$$A + ne^- \rightarrow D \qquad (1.3)$$

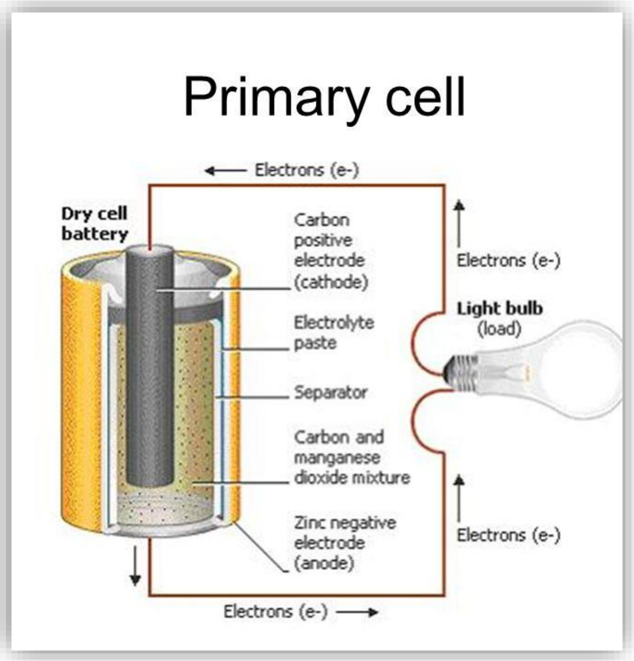
Primary cell
Electrons (e-)
Dry cell battery
Carbon positive electrode (cathode)
Electrolyte paste
Separator
Carbon and manganese dioxide mixture
Zinc negative electrode (anode)
Electrons (e-)
Light bulb (load)
Electrons (e-)
Electrons (e-)

Figure 1-4 Schematic of primary battery [6].

Batteries can be classified in numerous ways, some of them are:

- Primary (single use) versus secondary (rechargeable, multiple uses).
- Stationary systems (where electrodes do not move) versus flow systems (where the redox moieties are in solution phases).
- Li batteries (where Li-metal is the anode material) versus Li-ion batteries (where Li anode is replaced by intercalation compounds, alloys or even by transition metal compounds where the transition metal is in a low oxidation state).
- Metal-air batteries
- Aqueous versus non-aqueous batteries which have to use polar-aprotic electrolyte solutions due to reactivity considerations
- Miscellaneous

- Solid state batteries: there are lithium batteries containing solid-state electrolyte systems, based on Li-ions conducting ceramic or polymeric matrices. There are also high-temperature Na-S systems which use sodium ions conducting solid electrolyte matrices.
- Thermal reserve batteries: these are lithium batteries which are designed to work at high-temperature, on demand. They have mostly been exploited for military purposes [7, 8].

1.2.2 Super-capacitors

These devices include pairs of electrodes with high-surface-area, highly porous, made of activated (most often) amorphous carbons. Polarization of these pairs of electrodes in electrolyte solutions allows charges storage by electrostatic interactions, within the double layer at the electrode and solution interfaces. The interactions are purely electrostatic. That happens because the potential applied to the cell is no longer than this from the electrolyte solution. The pure electrostatic storage leads to the production of low energy density, but in turn leads to very high rates (high power density), very impressive stability and very prolonged cycle life. The energy density of such systems is proportional to ΔV^2. Therefore, it depends very strongly on the nature of the electrode solutions. The rate capability and capacitance of super-capacitors are the highest with aqueous solutions.

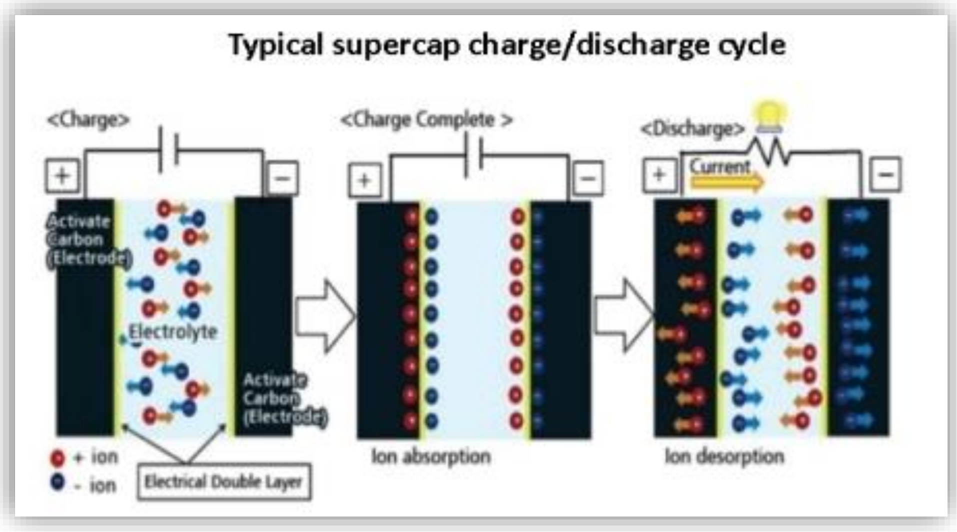
Typical supercap charge/discharge cycle
<Charge>
<Charge Complete >
<Discharge>
+
−
Current
Activate Carbon (Electrode)
Electrolyte
Activate Carbon (Electrode)
+ ion
- ion
Electrical Double Layer
Ion absorption
Ion desorption

Figure 1-5 Schematic of charge/discharge cycle of a typical super-capacitor[9].

There are further developments of pseudo-capacitors in which electrodes also contain components that undergo fast and highly reversible redox interactions, especially in aqueous solutions. High capacity and power density may be obtained with electrodes comprising MnO_2, MoO_3, RuO_2 and other metal oxides in which the metal changes its oxidation state in a fully reversibly manner (similar to the behavior of intercalation electrode materials).

Another further development of super-capacitors is asymmetric capacitors that have been developed. Here, capacitive charge exchange by electrostatic interactions occurs at one electrode, while the other electrode is a regular redox battery electrode. Such systems may exhibit high rate performance and prolonged cycle life as that of super-capacitors but show a clear advantage compared with super-capacitors in terms of energy density [7, 8].

1.2.3 Photovoltaic cells

Solar energy conversion directly to electricity is usually accomplished by using photovoltaic cells. PV modules produce electricity directly from sunlight with no pollutant emissions, vibration or noise. Photovoltaic cells (PV) make use of the photovoltaic effect. That effect depends on interaction of photons, with energy from sun radiation equal to, or more than the band-gap of PV materials. Some of the losses caused by the band-gap limitations can be avoided by overlapping semiconductors which have different band-gaps. Sunlight might be free, but power generation from sun radiation, with the use of photovoltaic cells cost is exceptionally high, although prices are starting to decrease. Solar energy has low energy density because PV-modules require a big enough surface area for producing small amounts of energy. The primary component that used in grid-connected PV-systems, is the inverter. The inverter is a device that converts DC power generated by PV-array into AC power consequent, with the power quality and the voltage requirement of the gird.

Silicon solar cells are considered to be the simplest and those that used the most on terrestrial and space applications. The photovoltaic system is a promising source for CO_2 emission reduction and electricity generation for energy resource saving, even if current technologies are applied. Further development in efficiency of photovoltaic cells, on their design for maximum use of recycled materials and also on the amount of material used will reduce their high cost, the energy requirement and greenhouse gas emissions [1].

1.2.4 Fuel cells

Fuel cells are electrochemical devices that transform chemical energy from fuels such as methanol and hydrogen into direct current (DC) electricity by electrochemical reactions with oxygen from the air. The first fuel cell was invented by Sir William Grove more than 150 years ago as a “gaseous voltaic battery”. He made the discovery that electricity could be generated by reversing the water-electrolysis with the usage of oxygen and hydrogen. The term “fuel cell” was first brought into existence by Mond & Langer almost half a century later.

Since fuel cell’s procedures do not contain combustion at all, it is more efficient, with no noise production, than the equivalent-power thermal generator. Furthermore, it is also a clean technology because the byproducts of the electrochemical reaction are only heat and water, when pure hydrogen is used as a fuel. All these make fuel cells a very competitive technology for reducing carbon emission intensity. There are six main types of fuel cells:

1. Phosphoric acid fuel cells (PAFCs)
2. Solid oxide fuel cells (SOFCs)
3. Alkaline fuel cells (AFCs)
4. Proton exchange membrane fuel cells (PEMFCs)
5. Direct methanol fuel cells (DMFCs)
6. Molten carbonate fuel cells (MCFCs)
7. Microbial fuel cell (MFCs)

The last one is receiving greater interests from fuel cell researchers in recent years.

The basic designs of all fuel cells are almost identical with differences in the electrolyte and the fuel used.

PEMFCs are the most promising from all fuel cell technologies. That is a consequence of their ability of working in low operating temperature, their quick start-up capability, low noise, light mass and high-power density. PEMFCs have been developed for use in small residential units like in distributed power generators in hotels, office buildings and hospitals, because of their compact design (1kW-5MW). Also, those are used in smaller scale like in portable electronic devices such as mobile phones, laptops, and video recorders because they are smaller and lighter, have faster response time and longer operating time compared to batteries and do not need recharging from the grid (20-100mW).

As we can understand PEMFCs have passed demonstration phase and are starting to move into the commercialization phase, a wide range of challenges still need to be overcome before PEMFCs entering the commercialization phase. Today, research on PEMFCs focuses mainly on improving PEMFC performance while cutting down cost by reducing the cost of catalysts used and mainly the amount of Pt catalyst, developing cheaper alternative materials for bipolar plates and membranes, performing steady-state system analyses, and hybridizing of the PEMFC system [10].

1.2.4.1 Basic structure and materials of PEMFCs

The basic PEMFC stack composed of membrane-electrode assemblies (MEAs) that are surrounded by bipolar plates. Those bipolar plates are sandwiched by current collector plates at both ends, sealed by gaskets and secured by several nuts and bolts.

The MEAs inside of the PEMFC, consist of the proton exchange membranes sandwiched by two types of electrodes: the one working as the anode electrode and the other working as the cathode electrode, where electric power is generated from the electrochemical redox reactions, whenever air and hydrogen are supplied.

The bipolar plates are usually manufactured by low porosity polymer-graphite composites, distribute hydrogen and air equally across the anodes and the cathodes of the MEAs respectively via flow fields or machine or moulded gas channels and conduct electrons through adjoining anodes and cathodes. The flow field can be parallel, straight, inter-digitated, serpentine or pinned.

The gaskets seal the stack of PEMFC and prevent leaking of gases or inter-mixing caused by leaking between plates, which may lead to hazardous conditions. The current collector plates transfer the electrical current from the anode to the corresponding cathode via loading. During the process electrical power is produced.

The electrodes at the MEA are usually consist of a gas diffusion layer made of cloth or carbon paper, and a catalyst layer composed of catalyst such as Pt (most commonly used) at the anode and Pt_xM_y (where M is a transition metal) at the cathode, which are impregnated on carbon materials such as graphitized carbon black (GCB), activated carbon (ACs), carbon nanofibers (CNFs) and carbon nanotubes (CNTs).

1.2.4.2 Working principles of PEMFCs

First, when the PEMFC stack starts its function, hydrogen and air are fed at a specific stoichiometric ratio and they are reacted to generate electrical energy and water.

1. At the anode, the hydrogen oxidation reaction (HOR) occurring, in the presence of the Pt catalyst is given by:

$$H_2 \rightarrow 2H^+ + 2e^- \tag{1.4}$$

2. At the cathode, the oxygen reduction reaction (ORR) occurring, in the presence of Pt_xM_y catalyst is given by:

$$4H^+ + 4e^- + O_2 \rightarrow 2H_2O \tag{1.5}$$

As we can see, the overall reaction of the PEMFC is:

$$2H_2 + O_2 \rightarrow 2H_2O \tag{1.6}$$

The proton exchange membrane is usually an impermeable to gas and electron proton conducting polymer (such as Nafion), which allowing the passage of protons and keeps gas crossover and electron short circuit to the minimum prices. Its effective operating temperature touch the price of 80-90 °C. The membrane conducts protons from the anode to the cathode in order to complete the electrical circuit with electrons that are conducted from the anode through the external load to the cathode, where both react with oxygen and form water.

A single fuel cell produces the theoretically amounts of electrical potential, 1.23 V, when in open circuit. This amount decreases, when connected on the load, and the usual operating voltage ranges from 0.6 to 0.7 V. The voltage loss is caused by several factors:

- activation polarization caused by slow electrochemical reactions at both the anode and the cathode
- ohmic polarization losses caused by hydrogen crossover or electron short circuit through the membrane
- mass transport polarization caused by hydrogen and oxygen concentration gradients at both electrodes, when both reactants are consumed rapidly and ohmic losses caused by the internal resistance of the cell.

CHAPTER II

2 PEMFC

2.1 General information and commercialization of PEMFCs

Polymer electrolyte membrane fuel cells (PEMFCs) convert the chemical energy, directly and efficiently to electrical energy. The chemical energy is stored in hydrogen fuel and water is the only by-product of the process described. Even when the hydrogen must be sourced from fossil fuels, the high efficiency of FCs compared to internal combustion engines offers the advantage of reduction in carbon dioxide emissions in transportations.

They have a unique package of advantages for use in vehicles:

1. a sufficiently low working temperature (80ºC)
2. quick start up
3. good energy density compared to other fuel cell types
4. relatively simple structure and mechanics
5. ability to work with pure hydrogen as a fuel, therefore emitting no CO_2 and the ability to use ambient air as the oxidant.

Other applications include stationary and portable power generation. Most major motor companies work only on PEM fuel cells due to their high-power density and excellent dynamic characteristics in comparison with other types of fuel cells. Examples of fuel-cell vehicles (FCV): DaimlerChrysler NeCar4a, GM Hydrogen 1, Toyota FCHV, Ford Demo IIa (Focus), Honda FCX-V3, VW Bora HyMotion, Nissan XTERRA FCV, and Hyundai Santa Fe

FCV. Auto makers such as Hyundai, Daimler, Toyota, Honda, and General Motors (GM) have announced plans of commercializing their fuel-cell vehicles since 2015 [11].

2.2 Working principles of PEMFC-H_2

Hydrogen gas insert to the anode where it is adsorbed onto the catalyst's surface. Each adsorbed hydrogen atom loses an electron (e^-) and is released from the metal surface as proton (H^+). The electrons flow to the cathode, through an external circuit, as current and the protons flow towards the cathode across the PEM. To the cathode where air is fed, oxygen is adsorbed onto the catalyst's surface. This bounded oxygen is next protonated by the incoming protons of hydrogen (H^+) and reduced by the incoming electrons. Finally, water is produced and then released from the catalyst surface. The hydrophobic nature of the surrounding media forces this water to exit the fuel cell. The catalyst used for both the hydrogen oxidation reaction (HOR-occurring at the anode) and the oxygen reduction reaction (ORR-occurring at the cathode) is Pt. Usually we deposit the Pt catalyst's small particles on the surface of larger carbon particles that act as a support.

- **Anode Processes**

Hydrogen is fed into the fuel cell as gas and reaches the anode where the HOR takes place. The hydrogen is adsorbed onto the surface of the Pt-electrode. Here occurs the breaking of hydrogen–hydrogen bond to give adsorbed atomic hydrogen (H*) [12], Equation(2.1):

$$\frac{1}{2}H_2 + * \rightarrow H^* \qquad (2.1)$$

(where * means a surface site).

The following loss of an electron from each hydrogen atom adsorbed, leads to hydrogen leaving the surface as protons (H^+), Equation (2.2):

$$H^* \rightarrow H^+ + e^- + * \qquad (2.2)$$

In PEMFC, the HOR's kinetics on a Pt electrode are very fast. Voltage losses are very small even for low Pt loadings (less than 5 mV for Pt anode loadings 0.05 mg cm^{-2}) [13].

- **Cathode Processes**

At the cathode, oxygen reduction reaction occurs and has a more complicated mechanism and it is known for its slow kinetics [14]. The ORR is the major challenge for PEMFCs because the catalyst material has to be stable enough and also chemically active in order to activate O_2. More than half of the voltage loss attribute to the ORR for a PEMFC system [15].

There are two pathways by which ORR can occur in acidic media [12].

First mechanism, follows a four-electrons-transfer process that leads to direct formation of water. First O_2 is adsorbed to the metal surface where oxygen–oxygen bond breaks to produce adsorbed atomic oxygen (O*), Equation (2.3):

$$\frac{1}{2}O_2 + * \rightarrow O^* \tag{2.3}$$

These single oxygen atoms O^*, are protonated by the hydrogen protons H^+, that flow across the PEM and reduced by the flowing electrons to give hydroxyl (OH*) [14] groups, Equation (2.4):

$$O^* + H^+ + e^- \rightarrow OH^* \tag{2.4}$$

Then further reduction and adding of protons occurs to the surface bound OH* in order to give water, Equation (2.5):

$$OH^* + H^+ + e^- \rightarrow H_2O + * \tag{2.5}$$

In the second pathway the O=O bond does not break upon O_2 adsorption to the metal surface (Equations (2.6) to (2.7)):

$$O_2 + * \rightarrow O_2^* \tag{2.6}$$

$$O_2^* + H^+ + e^- \rightarrow HO_2^* \tag{2.7}$$

This alternative route is observed to give H_2O_2. The details are unclear, but the reaction may proceed as follows (Equation (2.8)):

$$HO_2^* + H^+ + e^- \rightarrow H_2O_2^* \tag{2.8}$$

The H_2O_2 reacts further or may be desorbed (Equation (2.9)):

$$H_2O_2^* \rightarrow H_2O_2 + * \tag{2.9}$$

Generation of H_2O_2 in PEMFCs is highly undesirable as it causes degradation of the membrane [14]. As a result, a good catalyst should produce small amount or no H_2O_2.

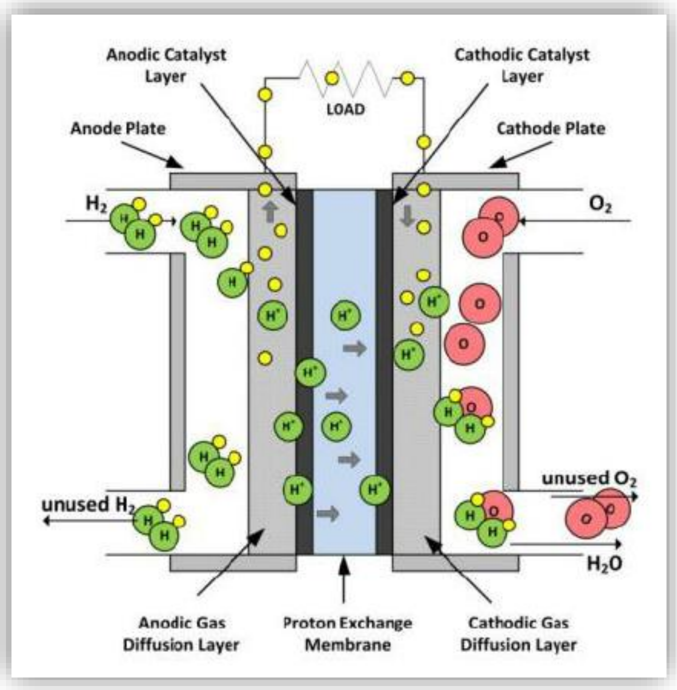
Anodic Catalyst Layer
Cathodic Catalyst Layer
LOAD
Anode Plate
Cathode Plate
H_2
O_2
H
H^+
O
unused H_2
unused O_2
H_2O
Anodic Gas Diffusion Layer
Proton Exchange Membrane
Cathodic Gas Diffusion Layer

Figure 2-1 A schematic of a proton exchange membrane fuel cell [16].

Figure 2-1 shows how a PEMFC-H_2 works.

There are four main essential characteristics of an effective PEMFC catalyst:

1. Stability - be durable to the operating environment in a fuel cell, including an acidic environment, strong oxidants, high and rapidly fluctuating temperatures, and reactive radicals, all these under an applied voltage.
2. Activity - the ability to adsorb the reactant not so strongly that the catalyst becomes blocked for the rest reactants or products, but strongly enough to facilitate the reaction.
3. Poisoning resistance - be resistance to poisoning by impurities that may be found in the feed gases and in the fuel cell itself.
4. Selectivity - to produce the desired product and minimize the undesirable side products and intermediates.

2.3 Why pure Pt is used as a catalyst

PEMFCs currently use Pt as the catalyst both at the anode and at the cathode. For heterogeneous catalysis, the catalyst must adsorb species on the metal surface with the desirable strength

- sufficiently enough, so the chemical bonds will break.
- weakly enough, so the product released when the reaction is done.

If the bond is too strong, the surface of the catalyst will quickly become blocked and the reaction will stop. If the bond is too weak, the substrate will not be adsorbed well on the catalyst and the reaction will not take place or be very slow.

The Sabatier principle gives the ideal interaction between substrate and catalyst as a balance between those situations described before. This principle is best explained by Balandin’s volcano diagrams. Those plot the catalyst activity against adsorption energy for a given reaction. As described, too strong or too weak a catalyst–substrate interaction gives a low catalytic activity. Therefore, the diagrams show an optimal binding that appears in a clear activity peak [14].

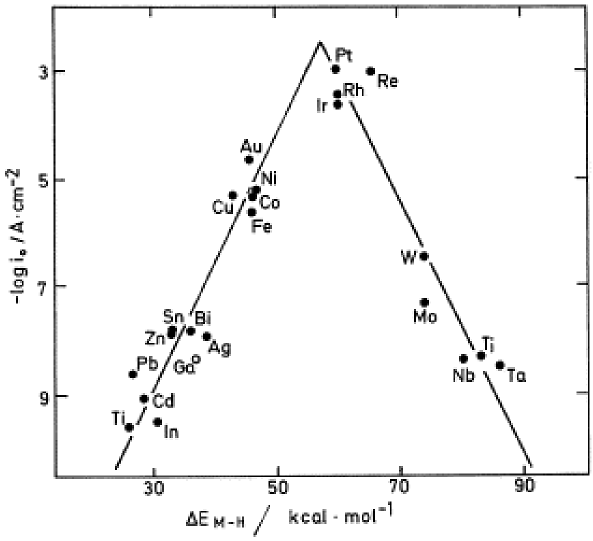

Figure 2-2 Pt has the highest activity of all bulk metals for hydrogen bonding energy[14].

From the Figure 2-2 we understand why Pt is currently used as the anode catalyst for HOR and why we need the reduction to the cost of fuel cell’s materials. The HOR is extremely quick and already requires much lower Pt loadings than the ORR.

2.4 Hydrogen fuel and impurities

Polymer electrolyte membrane fuel cells (PEMFCs), could ideally perform when pure hydrogen is the fuel. Although, for many (especially mobile) applications, pure hydrogen is not yet an existing option, because of the luck of availability and the pure storage techniques. Meantime, an obvious choice is on-site generation of hydrogen by steam reforming of many organic fuels (methanol, natural gas, gasoline, etc.). The reformate gases contain, besides hydrogen, also impurities such as carbon dioxide, small amount of carbon monoxide (CO), traces of hydrogen sulphide (H_2S) and ammonia (NH_3) and some other sulfur, carbon and nitrogen oxides (SO_x, CO_x, NO_x). PEMFCs conventionally operate around 80°C. At this temperature a CO concentration as low as 10-20 ppm in the gas feed cause a significant loss in fuel cell performance, as a result of CO-poisoning of the electrode catalyst [17].

2.5 Catalysts and CO-poisoning

An effective catalyst must show a significant resistant to the poisoning caused by impurities, which found in the fuel cell itself and also in the feed gases. Impurities in both the air streams and the hydrogen may have a negative impact on the performance of a PEMFC. All catalysts used are sensitive to poisoning. There are so many different poisoning mechanisms and poisons, that is very hard to make absolute ranking for evaluation of catalysts appropriateness.

Most harmful for Pt that used in PEMFC applications are sulfur species (SO_x) and carbon monoxide (CO) [17]. Pt as a catalyst is neither the most durable nor the most sensitive metal for operation with these or other poisons. In fuel cell applications, and also in other applications with Pt as catalyst, there are two methods of protection:

1. keep the impurities out of the system and
2. alloying the catalyst (Pt) with other metals to limit susceptibility to poisoning.

There are some strict quality specifications that have been agreed to be applied, for hydrogen intended for use in PEMFCs for transportation applications. However, improved resistance to poisons will still be a challenge, in order to avoid any low-quality batches of hydrogen that may cause irreversible damage to PEMFCs.

It has been also identified that the membrane electrode assembly (MEA), is the fuel cell’s component that is most affected by a contamination process. Three main effects have been identified:

1. kinetic effect - caused by poisoning of the electrode catalysts,
2. conductivity effect - detection of increase in the solid electrolyte total resistance, (including that of catalyst layer ionomer and of the membrane),
3. mass transfer effect- mass transfer problem caused by hydrophobicity changes and catalyst-layer structure.

Supported or unsupported Pt-based alloy catalysts have already been proven to exhibit high-tolerance to CO-poisoning. These catalysts include Pt-based metal oxide catalysts, binary, ternary and quaternary Pt-alloys, organic metal complexes and Pt-based composites [17].

2.6 Poisoning mechanisms

1) Pure hydrogen as a fuel

On the anodic platinum catalyst, oxidation of hydrogen takes place in two steps,

1. dissociative chemisorption, that requires two free continuous sites on the platinum surface. Equation (2.10)
2. electrochemical oxidation of hydrogen atoms that have been chemically absorbed, that requires two electrons, two free sites of the platinum surface, and two electrons. Equation (2.11).

$$H_2 + 2Pt \rightarrow 2Pt - H_{ads} \tag{2.10}$$

$$2Pt - H_{ads} \rightarrow 2Pt + 2H^+ + 2e^- \tag{2.11}$$

When pure hydrogen oxidation happens, both steps 1 and 2 are very fast, corresponding to a large exchange current density. The anode of a PEMFC, where HOR taking place, exhibits an overpotential (under operational conditions) of less than 100 mV.

2) Reformed hydrogen as a fuel (or in general hydrogen with impurities)

When the hydrogen gas contains carbon monoxide (CO), CO competes with hydrogen for which is going to be absorbed o the platinum's sites. Two types of bonding modes for the adsorbed CO molecules have been suggested, as shown in equations (2.12) and (2.13).

1. The linear-absorbed carbon monoxide species that involves one adsorption site per CO molecule.
2. And the bridge-bonded carbon monoxide species that requires two continuous platinum surface sites.

The adsorption occurs not only on free platinum sites, but also in platinum sites that there is H atoms. Equations (2.14), (2.15)

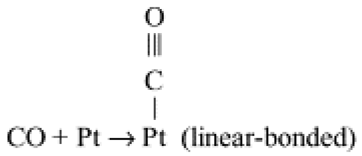

$$\mathrm{CO} + \mathrm{Pt} \rightarrow \overset{\substack{\mathrm{O}\\ |||\\ \mathrm{C}\\ |}}{\mathrm{Pt}} \ \text{(linear-bonded)} \qquad (2.12)$$

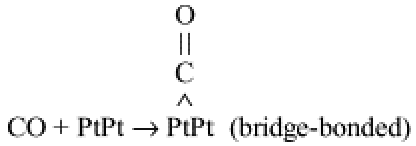

$$\mathrm{CO} + \mathrm{PtPt} \rightarrow \overset{\substack{\mathrm{O}\\ ||\\ \mathrm{C}\\ \wedge}}{\mathrm{PtPt}} \ \text{(bridge-bonded)} \qquad (2.13)$$

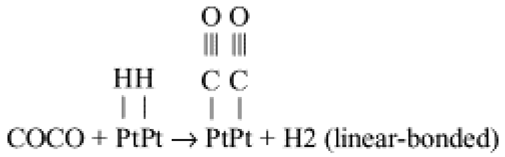

$$\mathrm{COCO} + \overset{\substack{\mathrm{HH}\\ |\ |}}{\mathrm{PtPt}} \rightarrow \overset{\substack{\mathrm{O}\ \mathrm{O}\\ |||\ |||\\ \mathrm{C}\ \mathrm{C}\\ |\ \ |}}{\mathrm{PtPt}} + \mathrm{H2} \ \text{(linear-bonded)} \qquad (2.14)$$

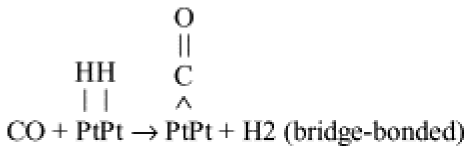

$$\mathrm{CO} + \overset{\substack{\mathrm{HH}\\ |\ |}}{\mathrm{PtPt}} \rightarrow \overset{\substack{\mathrm{O}\\ ||\\ \mathrm{C}\\ \wedge}}{\mathrm{PtPt}} + \mathrm{H2} \ \text{(bridge-bonded)} \qquad (2.15)$$

As we mentioned before, a popular method for improving the operation conditions of a PEMFC and the oxidation rate of H_2, with the presence of CO, is to use as CO-tolerant electrocatalysts as it is possible. Developing CO-tolerant catalysts is a major area of focus for mitigation contamination in PEM fuel cells. Pt-alloying with a second metal, called binary or more than one metal like ternary or quaternary, can give us catalysts that present more CO-tolerance than the pure Pt catalyst.

- Binary (PtM: where M= Mo, Nb, Ta, Sn, Co, Ni, Fe, Cr, Ti, Mn, V, Zr, Pd, Os, Rh).
- Ternary (PtRuM where M= Mo, Nb, Ta, Sn, Co, Ni, Fe, Cr, Ti, Mn, V, Zr, Pd, Os, Rh).
- Quaternary ($PtRuM_1M_2$ where M= RuMoNb).
- Pt-based metal oxide catalysts ($PtMO_x$ where M=W) [144 ($PtRuMO_x$ where M= Sn, W).
- Pt-based composite-supported PtRu-HxMO3/C (where M=W, Mo) and organic metal complexes [18].

Taking all those into account, in this study, we observe and test the CO-tolerance of Pt_xPd_y/C and Pt_xIr_y/C catalyst at PEMFCs-H_2 and low-temperature operation.

CHAPTER III

3 Theory of experimental techniques

In the current section the main theory of the experimental techniques that have been used in the current thesis, are referred and discussed. The as-used techniques are categorized to experimental techniques for physicochemical and electrochemical characterization.

3.1 Physicochemical characterization

3.1.1 X-Ray diffraction (XRD)

X-Ray diffraction is a very widely used technique for catalyst characterization. The very short wavelengths of X-rays are able to penetrate even solids and reveal their atomic structure, thus they are used to identify bulk phases and estimate their particle size [19].

The X-Ray diffraction method is based on the reflection of X-ray photons by the atomic planes. The angle θ with which they reflect it depends from their wavelength λ and the lattice spacing d (the distance between the atomic planed). The relation that links λ, θ, d all together is the Bragg's Law:

$$n\lambda = 2d \sin(\theta) \quad n=1,2,3.... \tag{3.1}$$

Each compound reflects the X-rays in a unique way thus each one has a unique diffraction pattern with different angles and intensities that can be transformed into atomic arrangements. The width of the diffraction peaks carries information about the size of the reflecting planes. The equation that relates width with crystal size is the Scherrer formula:

$$(L) = \frac{K\lambda}{\beta \ \cos\theta} \tag{3.2}$$

Where (L) is the volume-averaged thickness of crystallites, measured in a direction normal to the reflecting planes, *K* is a constant (often taken unity) and β is the peak width.

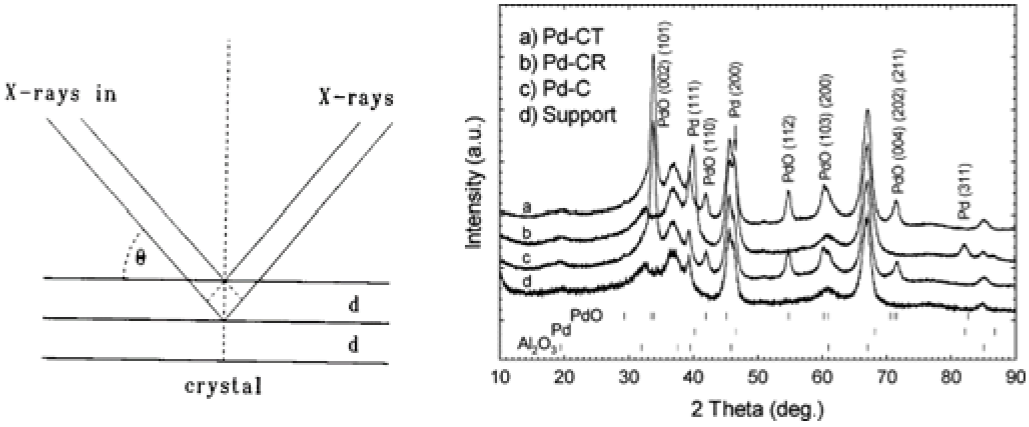

Figure 3-1 Reflected X-rays by atoms in a lattice plane interface constrictively in direction given by Bragg's Law (left) [19], XRD patterns of different catalyst (right) [20].

Despite the advantages of this technique there are some disadvantages. Because it is based on the interference between reflections of X-rays from atomic planes it requires samples with sufficient long-range order. Very small particles and amorphous phases give broad and weak diffraction lines or no diffraction at all, resulting in X-Ray diffraction able to detect only the larger particles. In some cases, there may be some overlaps with the diffraction lines from metals and the support. Finally, the surface region where the catalytic activity resides is virtually invisible for the X-Ray diffraction.

3.1.2 Transmission Electron Microscopy (TEM)

The transmission electron microscopy (TEM) is an analytical method in physical, chemical and biological sciences. TEM is a microscopy technique that uses a beam of electrons generated by thermionic emission from a filament. The electrons interact with the specimen as they pass through it and interact with it. The specimen is often ultrathin less than 100nm thick or a suspension on a grid. From this interaction an image is formed, focused and magnified at an imaging device. A transmission electron microscope is consist of several components-devices, like the electrons emission source for the generation of the electron beam, a vacuum system where the electrons travel, a series of electromagnetic lenses and electrostatic plates, an imaging device where the creation of the image takes place from the electrons that exited the system and a device that allow the insertion and removal of the specimens under study. The transmission electron microscopes are able of imaging at a very high resolution due to the small de Broglie wavelength of electrons. This enables the examination of single columns of atoms which are in the region of nanometers [19, 21].

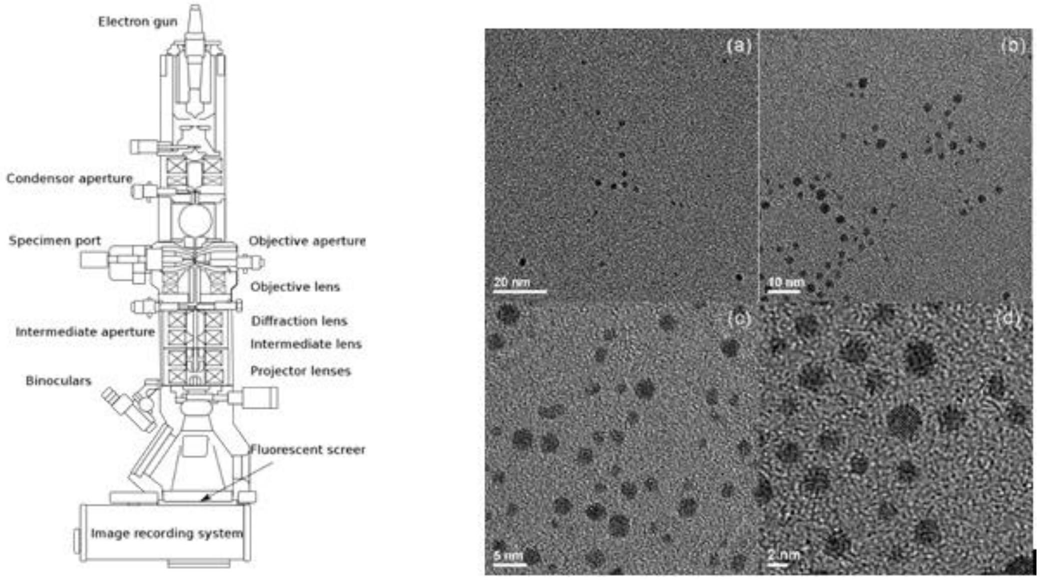
Electron gun
Condensor aperture
Specimen port
Objective aperture
Objective lens
Diffraction lens
Intermediate aperture
Intermediate lens
Projector lenses
Binoculars
Fluorescent screen
Image recording system
(a)
(b)
20 nm
10 nm
(c)
(d)
5 nm
2 nm

Figure 3-2 Transmission electron microscope and its components (left) [22], Series of typical phase-contrast TEM images of unsupported Au nanoparticles (right) [23].

3.1.3 Scanning electron microscopy (SEM)

Scanning electron microscopy is one of the most versatile techniques which allows the chemical composition characterization and the analysis and examination of the microstructure morphology.

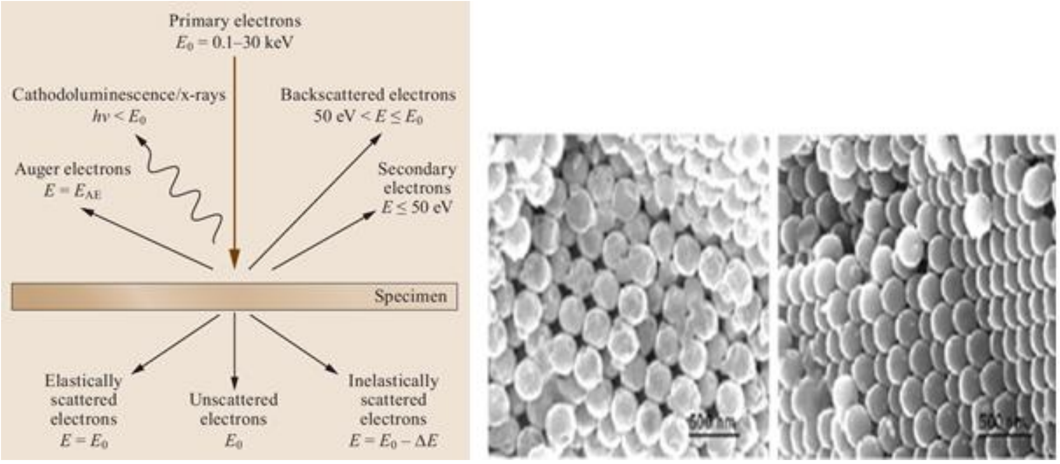
Primary electrons
$E_0 = 0.1–30$ keV
Cathodoluminescence/x-rays
$h\nu < E_0$
Backscattered electrons
50 eV $< E \leq E_0$
Auger electrons
$E = E_{AE}$
Secondary electrons
$E \leq 50$ eV
Specimen
Elastically scattered electrons
$E = E_0$
Unscattered electrons
E_0
Inelastically scattered electrons
$E = E_0 - \Delta E$
500 nm
500 nm

Figure 3-3 Working principles of SEM (left) [24], Examples of scanning electron micrographs (right) [25].

Scanning electron microscopy is a technique used to produce high resolution images of a sample surface area of about some nanometers in high vacuum. This can be achieved with the utilization of a high energy electron beam that interacts with the samples under investigation. As the beam of the electrons penetrate the sample and in dependence with the depth of the penetration a variety of signals are released. These can be backscattered electrons, Auger electrons, elastically scattered electrons and X-rays for example. The scanning electron microscopy uses the backscattered electrons and the secondary electrons, which they originate within a few nanometers from the surface. For the detection of these low energy electrons and the formation of a two-dimensional image of the surface there is need for photomultipliers. The intensity of the secondary electrons determines the brightness of the image. Thus, with the scanning electron microscopy one can extract morphological and topographical information about the surface under investigation, making this method the first step for the study of solids surfaces [21].

3.2 Electrochemical characterization

3.2.1 Rotating disk electrode technique (RDE)

The rotating disc electrode (RDE) is a hydrodynamic technique used in the three-electrode system and can provide kinetic information and limit the diffusion layer thickness due to forced convection. With it, it is able to precisely control the rotating speed therefore control the diffusion layer thickness, resulting in feasible quantitative analysis of the electrode reaction kinetics.

The advantages of this technique are the rapid establishment of a high rate of steady state mass transport, uniform mass transport on the electrodes surface, it gives good reproducibility and stable polarization curves. The disadvantages are first that the electrodes are not easy to construct, they are expensive and the theoretical treatment requires the determination of the solution flow velocity profiles (as functions of rotation rate, viscosities and densities) [26].

During the spinning of an RDE the disk works like a pump where it constantly feeds the electrode with fresh solution. The solution is pumped axially towards the surface of the electrode and then discarded centrifugally.

The RDE consists of a disk of electrical conductor (electrode) integrated in insulating material. The insulating material is Teflon, epoxy resin or other plastic (commonly used Teflon). The electrode is fastened to a motor in which we accurately control the rotating speed.

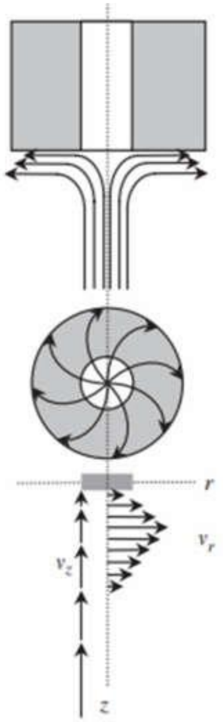

Figure 3-4 Streamlines for flow and vector representation of fluid velocities near the surface of a rotating disc electrode [27].

The equation that can help us extract the data we need is the so called Koutecký-Levich equation:

$$\frac{1}{i} = \frac{1}{i_k} + \frac{1}{B_L\sqrt{\omega}} \tag{3.3}$$

Where ω is the angular rotation rate of the electrode (rpm) and B_L is the Levich constant.

$$B_L = (0.620)nFAD^{\frac{2}{3}}v^{\frac{-1}{6}}C \tag{3.4}$$

Where n is the number of moles of electrons transferred in the half reaction, F is the Faraday constant (C/mol), A is the electrode area (cm^2), D is the diffusion coefficient (cm^2/s), v is the kinematic viscosity (cm^2/s) and C is the analyte concentration (mol/cm^3)

3.2.2 Cyclic Voltammetry (CV)

Cyclic Voltammetry (CV) is a versatile electro-analytical technique employed to investigate the reduction and oxidation processes of electroactive species. Its versatility combined with ease of measurement has resulted in extensive use of CV in the fields of electrochemistry, organic, inorganic, and bio-chemistry. The effectiveness of CV results from its capability of rapidly observing the redox behavior over a wide potential range.

Cyclic voltammetry is performed by repeatedly scanning the potential of an electrode, which is immersed in an unstirred solution, at a constant rate between two values and measuring the resulting current. The potential of the working electrode is measured against a reference electrode such as saturated calomel electrode (SCE). The controlled potential, which is applied to these electrodes can be regarded as an excitation signal. The potential is scanned linearly. The potential of the electrode sweeps between two values, the initial and the switching potential with a given scan rate of some mV/s. The resulting voltammogram is proportional of the scan rate, the greater the scan rate the sharper the curves of the voltammogram. The cyclic voltammogram is obtained by measuring the response signal which is the current at the working and counter electrode during the potential scan.

The voltammogram can be divided into two parts depending on the direction of the scan. The forward or cathodic scan, in which the potential is swept negatively from the initial to the switching potential and the backward or anodic scan, where the direction of the scan is switched to positive, so the potential can get its initial value.

A CV system consists of a potentiostat-galvanostat, a data recording system and the electrochemical cell where the half -cell reaction occurs. The electrochemical cell consists of an electrolytic solution, a working electrode (W), a counter electrode (C) and a reference electrode (R). The working electrode’s potential is varied linearly with time, while the reference electrode maintains a constant potential. The counter electrode conducts electricity from the signal source to the working electrode [28].

The purpose of the electrolytic solution is to provide ions to the electrodes during oxidation and reduction. A potentiostat is used to produce a potential which can be accurately determined, while allowing small currents to be drawn into the system without changing the voltage. The current-to-voltage converter measures the resulting current, and the data acquisition system produces the resulting voltammogram.

Cyclic voltammetry can provide qualitative information about electrochemical processes under various conditions, such as the presence of intermediates in oxidation-reduction reactions and the reversibility of a reaction. CV is also able to determine the electron stoichiometry of a reaction, the diffusion coefficients of the analyte, and the formal reduction potential, which can be used as an identification tool. In addition, because concentration is proportional to current in a reversible, Nernstian system, concentration of an unknown solution can be determined by generating a calibration curve of current versus concentration.

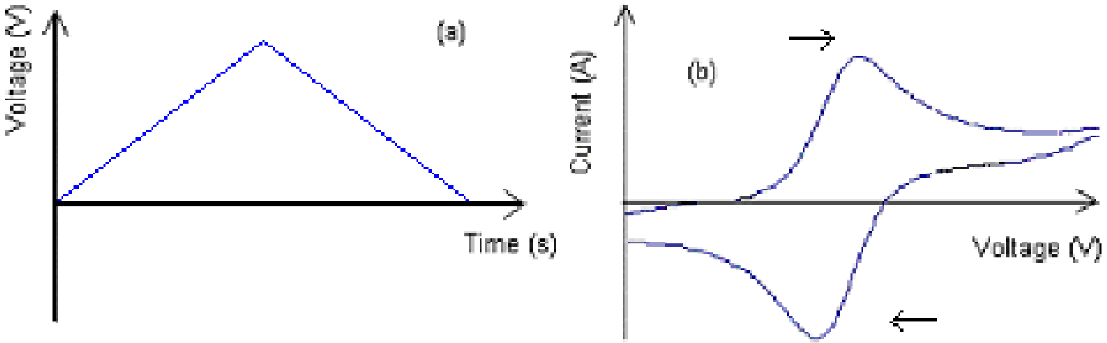

Figure 3-5 (a) The potential vs. time waveform and (b) a typical cyclic voltammogram of a oxidation-reduction process [30].

The equation that links the peak current of the resulting voltammogram and the scan rate is the Randles-Sevcik equation [29]:

$$i_p = 0{,}4463nFAC\sqrt{(\frac{nF\upsilon D}{RT})} \qquad (3.5)$$

Where i_p is the maximum current (ambers), n is the number of the electrons transferred in the redox event, F is the Faraday constant (C/mol), A is the electrode area in cm^2 , C is the concentration (mol/cm^3), υ is the scan rate (V/s), R is the Gas constant (J/K mol) and T is the temperature (K).

3.2.3 Chronoamperometry (CA)

Chronoamperometry is a potential step method which is time dependent and is used to study the kinetics of chemical reactions and the diffusion coefficients of electroactive species.

At the start of this method the initial potential which is applied, no redox reaction occurs and no current flows through the system. Then the potential takes a value able to start the electrochemical reaction. Reaction takes place at the electrodes surface and current start to flow. The reaction is restricted only by the diffusion of electroactive species. The current that is measured versus time indicates the depletion of the reactant over time.

The measured current can be described by the Cottrell equation:

$$\mathrm{i} = \frac{nFAc\sqrt{D}}{\sqrt{\pi\, t}} \tag{3.6}$$

Where i is the measured current in ambers, n is the number of electrons involved in the reaction, F is the Faraday constant (96485 C/mol), A is the area of the electrode(cm^2), c is the concentration of the electroactive species (mol/cm^3), D the diffusion coefficient for the species (cm^2/s) and the t is the time (s).

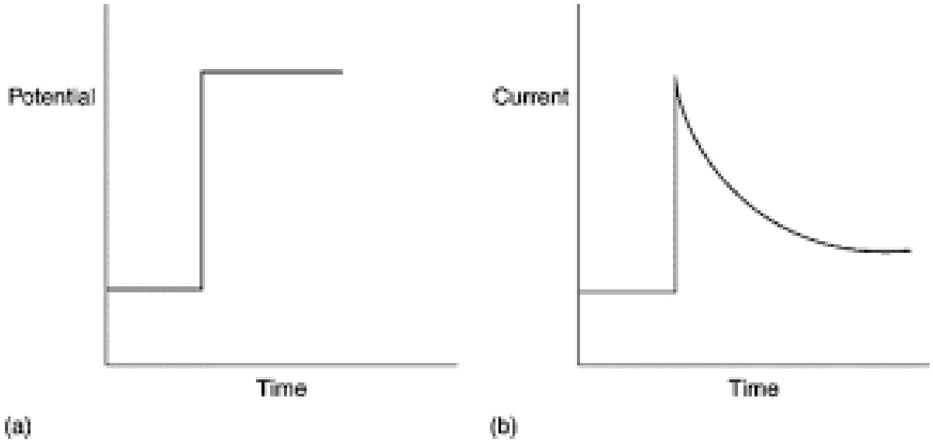

Figure 3-6 Single step chronoamperometry a) excitation waveform b) response waveform [31].

There are two types of this method single step and double step chronoamperometry, with the second one be able to determine the reversibility of the reaction under study by comparing the results of this method.

3.2.4 Linear Sweep Voltammetry (LSV)

Linear Sweep Voltammetry is a technique where the potential of the electrode is scanned and varies linearly with time. At the beginning of the measurement the potential takes a value where no reaction occurs thus no current exists. As potential change with time and take a certain value the reaction under investigation takes place and charge transfer begins. With the increase of the potential the current rises, where it makes a peak and afterwards start to decreases due to the depletion of the reactants.

Linear Sweep Voltammetry can be accomplished with the usage of a Rotating Disk Electrode which is submerged in the solution under study and constantly pumps fresh solution on the catalytic surface with the rotating speed affects the current measurements[32].

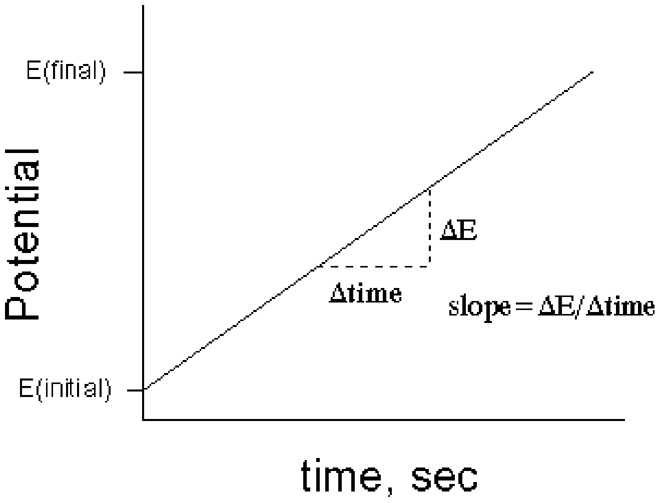

Figure 3-7 A typical voltammogram potential vs. time [33].

The measured current density is given by the Koutecký–Levich equation:

$$\frac{1}{i} = \frac{1}{i_k} + \frac{1}{i_{lim}} \tag{3.7}$$

Where i the measured current density, i_k is the

$i_{lim}$is the diffusion limited current and is given by the Levich equation based on mass transfer limited conditions:

$$i_{lim} = 0{,}21nFCD^{2/3}\sqrt{\omega}v^{1/6} \tag{3.8}$$

3.2.5 Electrochemical Impedance Spectroscopy (EIS)

Electrochemical impedance spectroscopy is an electrochemical technique that measures the impedance of a system in dependence of the AC potentials frequency. It allows the separation of the influence of different components such as electron transfer resistance and double layer capacity. It is a very sensitive technique that allows the observation of many changes that are difficult to see with other techniques. While resistance is the ratio of voltage or potential and current of a direct current (DC) system, the impedance is the ratio of voltage or potential and current for alternating current (AC) systems. The wave nature makes it necessary to define the impedance with two parameters, the total impedance Z and the phase shift Φ. The constant time shift between the periodic waves of current and voltage is called the phase shift Φ [34].

The total impedance is the ratio of the potentials amplitude and the currents amplitude. The resulting impedance is complex number, that can be expressed is the complex plane in polar coordinates by using Z as the length of the vector and Φ as the angle.

$$Z = Z' + Z'' \tag{3.9}$$

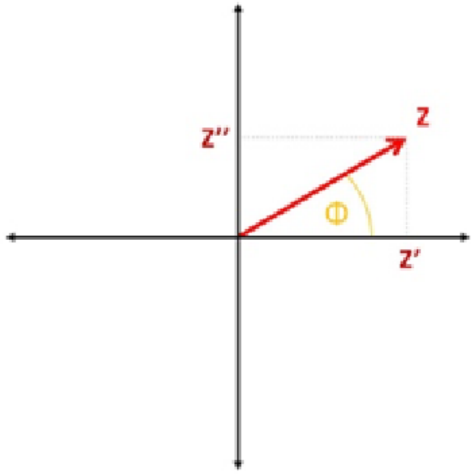

Figure 3-8 Impedance Z phase shift Φ, Z' the real part, Z'' the imaginary part of the impedance in the complex plane [34].

The impedance is measured by applying a potential wave to the working electrode and record the resulting current wave with the use of a potentiostat, which calculates Φ, Z', Z'' from these waves. The spectrum is made by measuring these parameters for potential waves with different frequencies.

Because most plots have logarithmic axis a fixed number per decade is chosen. For example, 10 frequencies between 10000 Hz and 1000 Hz, 10 between 1000 Hz and 100 Hz etc. these frequencies are usually equidistant on a logarithmic scale.

CHAPTER IV

4 Experimental part

4.1 Catalytic ink preparation

Each electrocatalyst powder consists of 20 w.t.% metal loading and was supported on carbon (Vulcan XC-72). For the preparation of the catalytic ink 5mg of the catalyst in the form of powder were mixed with 1.7 mL of deionized water, 0.3 mL isopropanol ($CH_3CHOHCH_3$) 10μL of 5 w.t.% Nafion solution. The mixture then was placed in the ultrasonicator where it stirred for 15 minutes until a homogeneous form was achieved. 10 μL of catalytic paste were deposited on the RDE surface, with a total area of $0.07 cm^2$. The metal loading on the geometric area of the RDEs surface was 71.4 $\mu g/cm^2$. Before the deposition all RDE were polished with deionized water and Aluminum oxide nano-powder (of particle size <50nm) and they were cleansed with alcohol. The electrodes dried up in the air for the duration of 4 hours in room temperature.

4.2 Electrochemical characterization

The three-electrode cell compartment is where the electrochemical experiments are conducted. This compartment consists of three electrodes, a working electrode (W), a counter electrode (C) and a reference electrode (R). All electrodes are immersed in the electrolyte solution. With a potentiostat it is able to control the potential between the working electrode and the reference electrode. During the three electrode experiments, current flow between the working and the counter electrode while the potential is measured with respect to the reference electrode. The counter electrodes are fabricated from electrochemically inert materials such as platinum gold or carbon. The counter electrode must have a high surface area much larger than the working electrode to ensure that the half reaction occurring at the counter electrode can occur fast enough so the process at the working electrode is not limited.

When electroanalytical chemistry is performed, the working electrode and the counter electrode provide a circuit over which current is either applied or measured. The potential of the counter electrode is rarely measured and adjusted to balance the reaction occurring at the working electrode. This configuration allows the potential of the working electrode to be measured against the reference electrode without compromising the stability of the reference electrode by passing current over it.

The counter electrode can be isolated from the working electrode by a glass frit to prevent byproducts that produced in this to contaminate the rest of the solution [35].

4.3 Experimental procedures

All electrochemical measurements were carried out with a potentiostat-galvanostat, workstation AMEL 7050 in a three-electrode cell compartment, with a Pt wire as the counter electrode and saturated calomel electrode (SCE) as the reference electrode. The working electrode was consisted of a rotating disk electrode of a 3mm diameter and a total area of 0.07 cm2. For all measurements the electrolyte that was used, was HClO4 with a concentration of 0.1 M. For all experiments the temperature of the cell was held at 30 °C via a thermostat.

4.3.1 Cyclic voltammetry

Before the solution was saturated with N_2 gas for 45 minutes in order to remove impurities and other gases like oxygen that were dissolved in the electrolyte. For the conditioning of the catalyst the RDE was placed on the holder. The electrodes before the measurements were conditioned for 45 minutes via cyclic voltammetry technique at a scan rate of 100 mV s^{-1} in 0.1 M $HCLO_4$ aqueous solution, saturated with N_2. In this technique the potential of the system is swept back and forth between two voltage limits while the current is recorded. The voltage swept is normally linear with time and the plot of the current versus voltage is called a cyclic voltammogram. The initial and the switching potentials in this method were 0.1V and 1.2V (vs. RHE) respectively. After the first part of the activation a second cyclic voltammetry treatment was performed for the determination of the electrochemical active surface area (ECSA). The initial and the switching potentials were the same but this time a scan rate of 50mV s^{-1} was applied.

4.3.2 Linear sweep voltammetry with rotating disk electrode

Before the application of the linear sweep voltammetry method hydrogen and a mixture of hydrogen and nitrogen at different proportions flowed through the electrolyte for 40 minutes, until saturation point was achieved and the OCV (open circuit voltage) stabilized. The LSV carried out with a cathodic scan rate of 5mV s^{-1} from the initial potential of 0.4 V to a final potential of 0 V (vs. RHE) for every experiment. Linear sweep voltammograms were taken before and after chronoamperometry at different rounds per minute (400, 1000, 1600, 2200 rpm).

4.3.3 Chronoamperometry

Before and during the application of the chronoamperometry technique for every catalyst the solution remained saturated with different hydrogen, nitrogen and carbon monoxide gas flow to get the desirable ppm of CO. With it is able to poison the catalyst with carbon monoxide and to check his stability during the measurement with the recording of current density and its decline over time. The applied potential step was -0,2V and the gas flow was H_2/CO (10/40 cc/min) for the durations of 3, 6 and 9 hours for all catalysts.

4.3.4 Electrochemical Impedance Spectroscopy

Before each measurement the resistance of every electrode was measured via electrochemical impedance spectroscopy (EIS). In order for the experiment to start the measured resistance should be lower than 10 Ohms.

4.3.5 Test of durability to CO in HOR

The following measurement protocol was established for the experimental investigation of the durability of Pt_xPd_y/C and Pt_xIr_y/C catalyst in the presence of 400 ppm CO:

1. Creation of an inert atmosphere with N_2 supply for a period of 45min.

2. Measurement of impedance (Ac=5mV, from 10.000 to 0.02 Hz, σε OCV). For the conduction of the experimental measurements the resistance between the electrode film and the solution should be less than 10 Ohm. Otherwise re-deposition will take place.
3. The catalyst activation is achieved via cyclic voltammetry method at 150 mV s^{-1} for half an hour.
4. Experimental blind measurement using cyclic voltammetry with a scan rate of 50mV s^{-1}. From the hydrogen adsorption and desorption surfaces the electrochemically active surface is calculated. The experimental measurement of the blind by using cyclic voltammetry with a scan rate of 50 mV s^{-1}. The electrochemical active surface area calculated from hydrogen adsorption and desorption surfaces.
5. Solution saturation with fuel (H_2 or H_2/CO (400ppm in N_2) or H_2/N_2) (1 hour).
6. Subsequently linear scan voltammetry (from 0 to 0.35 V vs. RHE) (5mV s^{-1}) is then performed with the aid of the rotating disk electrode technique (1600rpm). The fuel supply during the measurement is maintained at 50cc. In this way the catalytic activity is observed before the start of chronoamperometry.
7. Chronoamperometry is performed at -0.2V at 1600 rpm and 50cc fuel supply. The current is recorded for the time period until the current drops dramatically.
8. Step 6 is repeated and it is detected if there is a drop-in catalytic activity after chronoamperometry.
9. Solution saturation with N_2 (45 min).
10. Cyclic voltammetry measurement, with a scan rate of 50mV s^{-1}. The purpose of this measurement is to identify the adsorbed CO on the catalytic surface. It is noted that step 8 does not affect step 10 as the adsorbed CO is oxidized to 0.6V (vs. RHE), while step 8 is in the range of 0 to 0.35V (vs. RHE).

The results of the electrochemical analysis are shown in Figure 4-1. Based on the cyclic voltammetry (Figure 4-1a) the electrochemically active surface is calculated 33m^2 g^{-1}. Based on the results of chronoamperometry (Figure 4-1b) when pure hydrogen is supplied the current remains constant for approximately 6.5 hours. In the case of introduction of CO in the fuel, the current drops sharply at 1.5 hours, indicating catalyst poisoning.

4.3.5.1 Carbon monoxide coverage calculation

Carbon monoxide stripping is a method which, like its name say stripping of carbon monoxide, that has been electrochemically bonded to the catalyst active centers, takes place. This is accomplished with the application of the technique called cyclic voltammetry. From the resulting voltammogram one is able to see if carbon monoxide has been adsorbed, during chronoamperometry, because at the potential intervals where carbon monoxide oxidizes the voltammogram will show a peak. The size of which is proportional to the carbon monoxide that have been adsorbed.

To determine the carbon monoxide coverage over the catalyst, it's necessary the use of cyclic voltammetry, before and after the catalyst poisoning with carbon monoxide via chronoamperometry.

First one must utilize the cyclic voltammogram before the poisoning of the catalyst to determine the surface area S (cm^2) of the catalyst.

$$S = \frac{Q_H}{\theta_H \times 0.210 mCcm^{-2}} \tag{4.1}$$

Where Q_H is the charge in mC, $210mCcm^{-2}$ corresponds to a monolayer of adsorbed hydrogen and θ_H is the hydrogen monolayer coverage at end point potential which is 0.77.

The surface area that is covered by carbon monoxide S_{CO} in cm^2 was calculated as follows:

$$S_{CO} = \frac{Q_{CO}}{0.420 mCcm^{-2}} \tag{4.2}$$

Where Q_{CO} is the carbon monoxide stripping charge in mC, after correction with double layer capacitive current and the appropriate potential intervals, and $0.420mCcm^{-2}$ corresponds to the charge need to oxidize a monolayer of adsorbed carbon monoxide that is linearly bonded.The carbon monoxide coverage now can be calculated with the following equation:

$$\theta_{CO} = \frac{S_{CO}}{S} \tag{4.3}$$

Where S_{CO} is the carbon monoxide surface area, S is the surface area determined by the hydrogen adsorption method and θ_{CO} is the CO coverage (0< θ_{CO}<1) and is a dimensionless number.

CHAPTER V

5 Experimental results

5.1 Physiochemical characterization

Transmission electron microscopy (TEM) was performed with a Philips CM12 (0.2nm resolution) microscope equipped with a high-resolution camera with an acceleration voltage of 120 kV. X-ray diffraction (XRD) measurements were performed with a Rigaku Corporation diffractometer with CuKa radiation. Figures 5-1 and 5-2 illustrate micrographs by transmission electron microscopy for platinum-palladium and platinum-iridium, respectively.

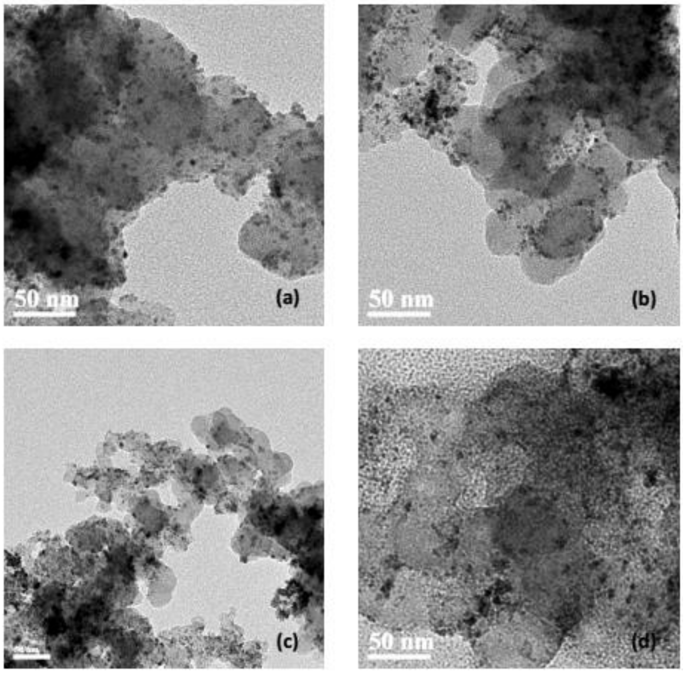

Figure 5-1 Transmission electron microscopy micrographs of: (a) Pd/C, (b)Pt_1Pd_3/C, (c) Pt_3Pd_1/C, (d) Pt_1Pd_1/C.

As illustrated in Figure 5-1 in all cases the distribution of the nanoparticles on the carbon substrate is uniform. The size of the nanoparticle ranges from 2-4nm for the bimetallic Pt_1Pd_3/C and Pt_3Pd_1/C, while for the Pd/C and Pd_1 Pt_1/C the particle size is slightly increased, taking the value of 4-6nm.

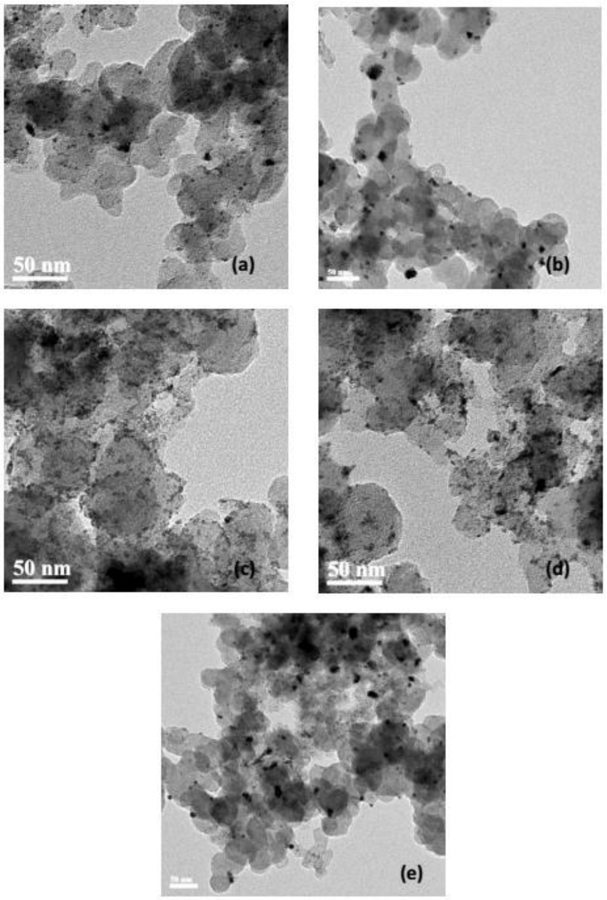

Figure 5-2 Transmission electron microscopy micrographs of: (a) Ir/C, (b) Pt/C, (c) Pt_1Ir_1/C, (d) Pt_1Ir_3/C, (e) Pt_3Ir_1/C.

In the case of bimetallic platinum-iridium catalysts, it is observed that as the amount of platinum increases, the size of the nanoparticles increases. The larger size of the nanoparticles also impedes their uniform distribution on the substrate. The smallest size of the nanoparticles is observed for Pt_1Ir_1/C and Pt_1Ir_3/C, with values of approximately 2-4 nm.

Figure 5-3 illustrates the results of X-ray analysis (XRD). It is found in all cases that an alloy is formed between the metals. In both cases of the bimetallic catalysts the typical orientations of the crystals are shown, as listed in each figure, but the intensity of each peak varies according to the ratio of the metals.

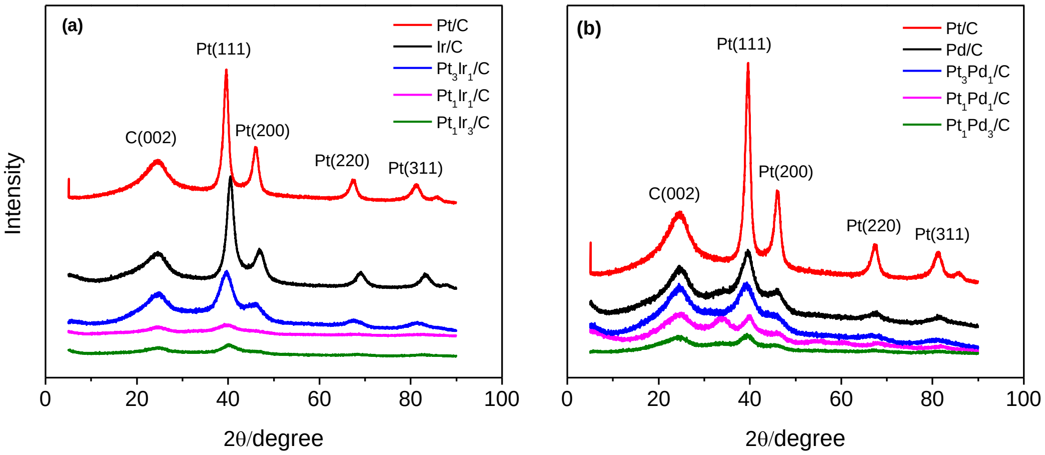

Figure 5-3 XRD analysis results, (a) Pt_xIr_y/C and (b) Pt_xPd_y/C.

In the case of the bimetallic Pt_xIr_y/C catalyst as the Pt / Ir ratio decreases it is observed that the crystalline peaks and the crystalline lattices (111) and (200) tend to be unified, indicating that crystalline amorphous increases [36].

Figure 5-4 illustrates the results of XPS and EDX analysis of the electrocatalyst samples.

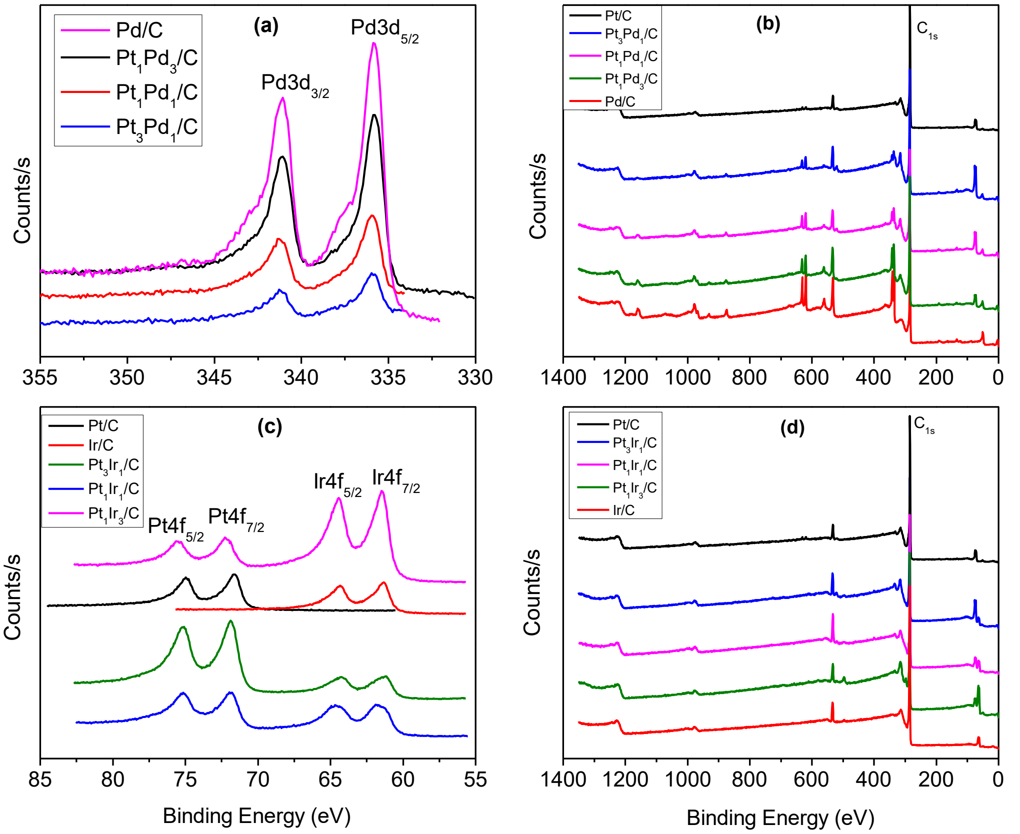

Figure 5-4 XPS and EDX analysis results.

The schematic representation of the Pt4f and Ir4f peaks (Figure 5-4 (c)) shows that as the percentage of Ir in the bimetallic catalyst increases, the binding energy (BE) values of Pt4f shift to more positive values. Conversely, as the percentage of Pt increases, Ir4f's BE shifts to more negative values.

These results indicate differences in the electronic structure of Pt after the alloy with Ir. In particular, the results may indicate that the intra-atomic charge transfer process from Pt to Ir is likely due to variations in the activation energies of the two metals [37]. Alternatively it can be explained by the increase in vacancy at the 5d orbital of Pt in the bimetallic catalysts[38].

In the case of Pt_xPd_y with the increase in Pd the Pt4f BE shifts to more negative values while in the reverse, while the Pt rate increases the Pd3d BE shifts to more positive values. This is also explained by differences in the electronic structures of the two metals after the alloy was created [39].

From the EDX diagrams, it appears that each electrocatalyst was successfully prepared, as for each case of bimetallic electrocatalyst it is confirmed that the molecular ratio of the metals is similar to the desired.

5.2 Electrochemical characterization

5.2.1 Catalyst activation

For the activation of the catalysts, after the establishment of an inert atmosphere with N_2 supply for a period of 45 min, they underwent cyclic voltammetry for half an hour at 150 mV s^{-1} for the electrochemical purification of the deposited catalyst at the electrode. This procedure is presented below (Figure 5-5). It is obvious that for (a), (c), (d), (e) and (f) catalysts, which they contain Ir, after the electrochemical purification the hydrogen adsorption and desorption peaks increased. For the (b), (g), (h) and (i) catalysts, which they contain Pd, the oxidants reduction peaks also increased.

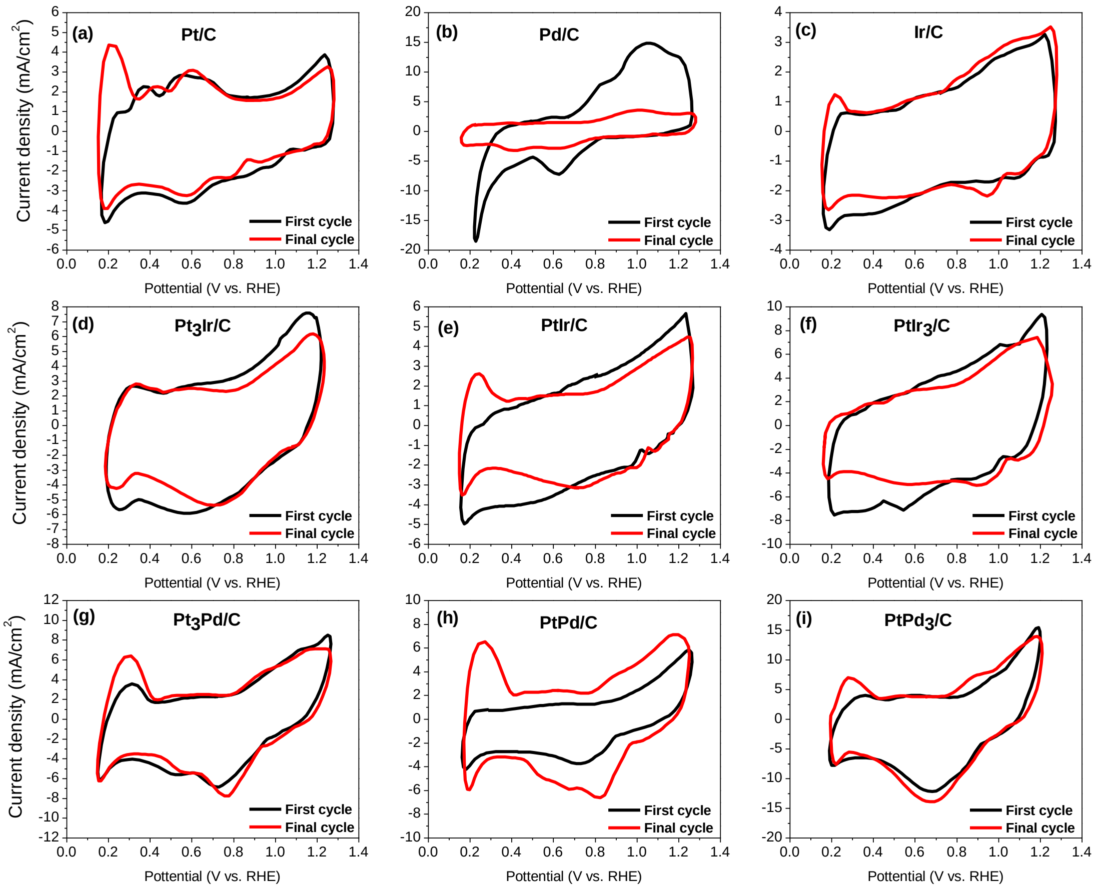

Figure 5-5 Activation-purification of the deposited catalysts.

5.2.2 Electrochemical active surface area (ECSA)

The electrochemical active surface area under working conditions can be determined by the hydrogen adsorption method which is obtainable via cyclic voltammetry technique. During the oxidation, hydrogen atoms are desorbed according to the following electrochemical reaction:

$$H_{ad} \rightarrow H^{+} + e^{-} \tag{5.1}$$

The measure of the number of electrons liberated during the oxidation of the metal (platinum, palladium and iridium) gives the number of hydrogen atoms desorbed and thus the number of adsorption sites present on the electrodes surface. This defines the active surface of the electrode.

The total charge corresponding to the hydrogen desorption can be related to the integral of the curve for a certain interval of potentials where the hydrogen atoms are being desorbed.

From the obtained integral the double layer capacitive current must be subtracted so the obtained charge is corresponded only to the charge due to desorbed hydrogen.

For the calculation of ECSA on catalysts the following equation is used:

$$ECSA = \frac{Q_H}{(a \times C_{M1} + b \times C_{M2}) \times m} \tag{5.2}$$

Where a and b are:

$$a = \frac{x}{x+y} \qquad , \quad b = \frac{y}{x+y} \tag{5.3}$$

With m (μg) be the mass loading of metal, x and y are the stoichiometric proportions of the corresponding metal and C_{mi} corresponds to a monolayer of adsorbed hydrogen on different metals. For platinum $210\mu C/cm^2$, palladium $205\mu C/cm^2$, iridium $218\mu C/cm^2$.

This equation can be simplified for the calculation of ECSA on platinum-based catalysts as follow with a slight deviation of the results:

$$ECSA = \frac{Q_H}{m \times C} \tag{5.4}$$

Where m (μg) is the mass loading of metal and C corresponds to a monolayer of adsorbed hydrogen and is $210\mu C/cm^2$. Q_H (μC/cm^2) is the measured hydrogen adsorption charge in the negative going scan after correction with the double layer charge.

$$Q_H = \int_{t_1}^{t_2} I\, dt = \frac{1}{v} \int_{E_1}^{E_2} I\, dE \tag{5.5}$$

Cyclic voltammetry technique was conducted under N_2-saturated 0.1 M $HClO_4$ aqueous solution for 5 cycles with a scan rate of 50 mV s^{-1}. From the following diagrams, called 'CV blinds', the ECSA of the catalysts under investigation, can be calculated.

Figure 5-6 (a) shows the electrochemical response of the Pt/C (pink line), Ir/C (green line), in comparison with Pt_3Ir/C (black line), PtIr/C (blue line) and $PtIr_3$/C (red line). There can be observed five main different zones:

1. zone of hydrogen desorption from 0.1 to 0.4 V (vs. RHE),
2. the zone free of faradaic processes, so called "double layer region" from 0.4 to ~0.6 V (vs. RHE),
3. the zone of surface platinum and iridium oxides formation from ~0.6 to 1.2 V (vs. RHE),
4. the zone of surface platinum and iridium oxides reduction from ~0.6 to 1.2 V (vs. RHE),
5. zone of hydrogen adsorption from 0.1 to 0.4 V (vs. RHE).

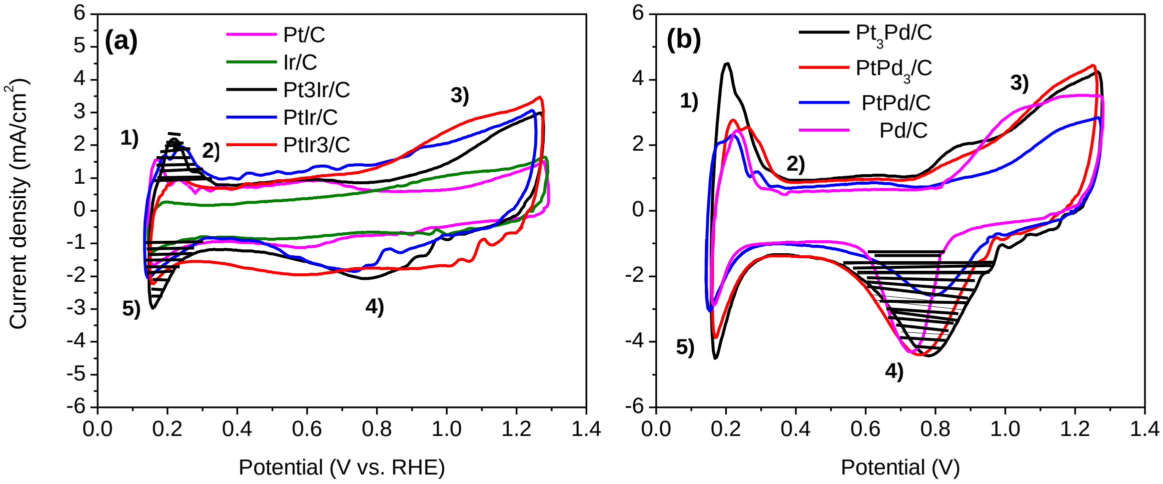

Figure 5-6 Cyclic voltammetry curve of 20 wt.% (a) Pt$_x$Ir$_y$/C and (b) Pt$_x$Pd$_y$/C for the hydrogen oxidation reaction, in a N$_2$ saturated 0,1 M HCLO$_4$ solution at a scanning rate of 50 mV s^{-1} , from 0.1V to 1.2V (vs. RHE), measurements were taken at 30^o C . The marked areas are used for the calculation of the ECSA.

For Pt$_x$Ir$_y$/C the charge consumed in adsorbed hydrogen oxidation, is calculated by integrating the voltammetry peaks in the hydrogen adsorption/ desorption region. In many cases, the charge caused by the anodic hydrogen desorption process is used. Ideally, both of these peaks should be the same, but in non-ideal cases those peaks present some differences and that is why we use the average price between adsorption and desorption charges to calculate the charge [40].

Figure 5-6 (b) shows the electrochemical response of Pt$_3$Pd/C (black line), PtPd$_3$/C (red line), PtPd/C (blue line) and Pd/C (pink line). There can be observed five main different zones:

1. zone of hydrogen desorption from 0.1 to 0.4 V (vs. RHE),
2. the zone free of faradaic processes, so called “double layer region” from 0.4 to ~0.7 V (vs. RHE),
3. the zone of surface platinum and palladium oxides formation from ~0.7 to 1.2 V (vs. RHE),
4. the zone of surface platinum and palladium oxides reduction from ~0.6 to 1.2 V (vs. RHE),
5. zone of hydrogen adsorption from 0.1 to 0.4 V (vs. RHE).

For palladium, hydrogen adsorption on the surface occurs at the same time with hydrogen absorption in the bulk and there is a difficulty on separate and recognize them. Therefore, it is not possible to take information about how hydrogen adsorption contributes to the overall charge and to determine the ECSA for a Pd electrode.

Therefore, it was suggested that the smaller hydrogen oxidation peak could be related to the current necessary for the oxidation of adsorbed hydrogen. The method that is more accurate for determination of the ECSA and used mainly for Pd, is integration of the surface oxide reduction[40].

The smaller peaks shown in these figures (Figures 5-6 (a), (b)), after the 1) and before 3) zone, are related with the consumption of other oxides that may be formed during the whole process.

From the integration of the appropriate peak for each catalyst, as mentioned before and with the suitable calculations (equations 5.2, 5.3, 5.4, 5.5) the following results for the ECSA are listed at Table 1.

Table 1: Electrochemical active surface area for Pt_xIr_y and Pt_xPd_y catalysts.

Electrocatalyst 20% wt	ECSA (m^2/g_{metal})
Pt/C	13.67
Ir/C	7.33
Pd/C	28.3
Pt_3Ir/C	32.39
PtIr/C	28.28
$PtIr_3/C$	11.43
Pt_3Pd/C	95.7
PtPd/C	68.15
$PtPd_3/C$	123.07

5.3 Linear sweep voltammetry results

5.3.1 Linear sweep voltammetry results for different flow rates of H_2/N_2

Furthermore, linear sweep voltammetry was performed, for the exploration of the most promising system, on a disk electrode with a thin layer of catalyst applied onto it. This method allowed the acquisition of quantitative data concerning the magnitude of the electrochemical activity and tolerance with respect to carbon monoxide in the catalyst under study. Figures 5-7, 5-8, 5-9 and 5-10 presents the polarization curves for the electrooxidation of hydrogen on a rotating disk electrode (0.07 cm^2) with thin layer (71.4 μgcm^{-2}) of the catalyst under investigation applied onto it, in different fuel proportion of H_2/N_2 and different rotation speeds. Well pronounced segments corresponding to the limiting current are observed in all polarization curved for all catalysts.

The HOR activity of the tested electrocatalysts was examined by rotating disk electrode (RDE) experiments, from which the corresponding linear sweep voltammetry curves (LSV) were taken. For the Figure 5-7, 5-8, 5-9, and Figure 5-10 all RDE experiments were conducted under H_2-saturated 0.1 M $HClO_4$ aqueous solution, at a scan rate of 5 mVs^{-1}, at rotation rates of 400 rpm, 1000 rpm, 1600 rpm, 2200 rpm. The observation of the LSV curves, leads to a classification of three different regions:

1. the diffusion control region, where the current is controlled by the mass transport processes,
2. the mixed region, where the current is controlled from both reaction kinetics and mass transport,
3. and the kinetic control region, where the current is controlled by reaction kinetics and the rotation rate does not have any impact.

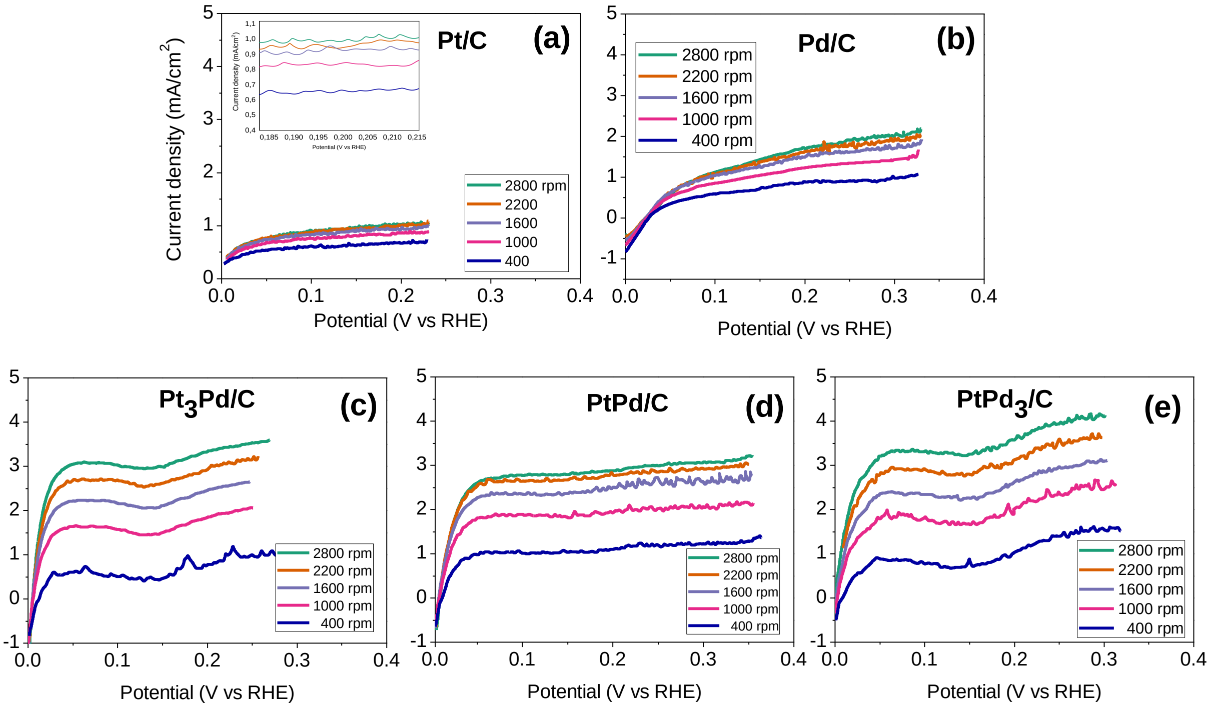

Figure 5-7 LSV curves in H2-saturated 0.1 M HClO4 aqueous solution, at rotation rates 400, 1000, 1600, 2200, 2800 rpm, at a scan rate of 5 mV s-1 for (a) Pt/C, (b)Pd/C, (c) Pt3Pd/C and (d) PtPd/C, (e) PtPd3/C2 before exposure to CO.

For the Pt$_x$Pd$_y$/C group of catalysts, illustrated at Figure 5-7, it can be observed that the diffusion control region is located at potentials above ~0.075 V (vs. RHE). The mixed-control region from 0.025 to 0.075 V (vs. RHE) and the kinetic control region from 0 to 0.025 V (vs. RHE). Also, it can be noticed that for catalysts with Pd-metal load the flat plateau cannot easily displayed. The wave distortion on linear sweep voltammograms at Figures 5-7, 5-10, observed from 0.1 to 0.2 V, on catalyst containing Pd can probably be referred to non-steady state oxidation of hydrogen dissolved in palladium. As it can be seen, Pt/C and Pd/C presents the lowest current density at the mass transport region (almost 0.99 mA cm^{-2} and 2 mA cm^{-2} for 1600 rpm at ~0.075 V (vs. RHE)), where the flat plateau is observed. Respectively, for Pt_3Pd/C the limiting current density at ~0.075 V (vs. RHE) is 2.65 mA cm^{-2}, for PtPd/C is 2.86 mA cm^{-2} and for $PtPd_3/C$ is 3.13 mA cm^{-2} (all the prices referred to 1600 rpm).

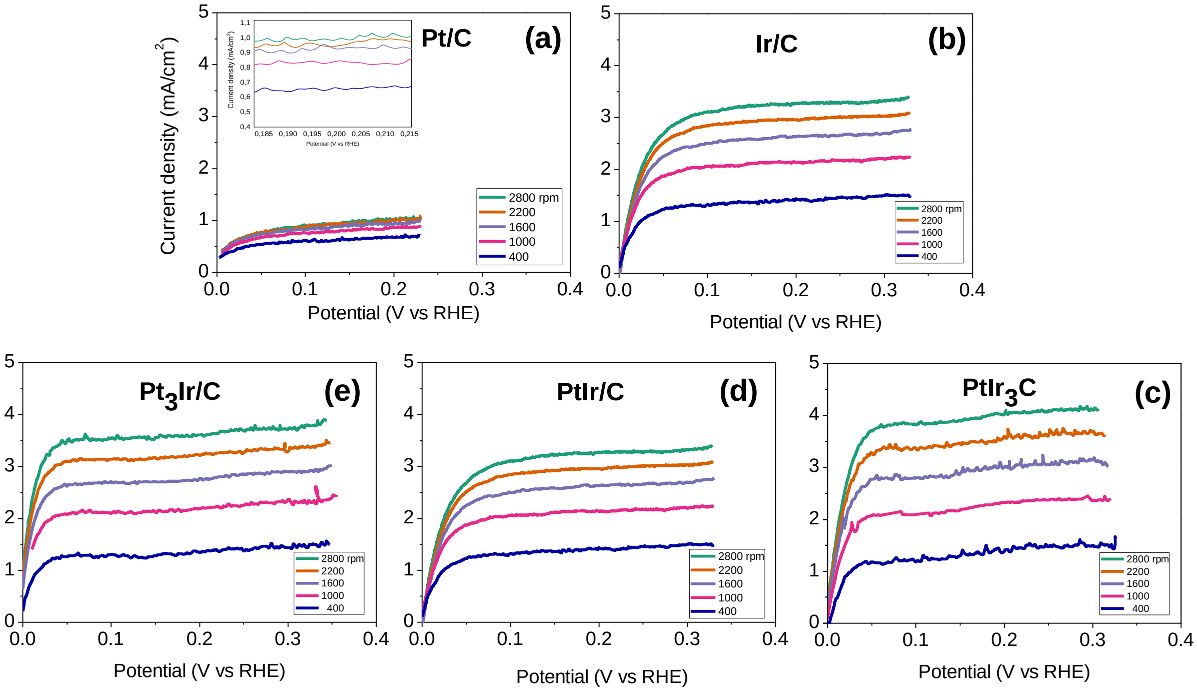

Figure 5-8 LSV curves in H2-saturated 0.1 M HClO4 aqueous solution, at rotation rates 400, 1000, 1600, 2200, 2800 rpm, at a scan rate of 5 mV s-1 for (a) Pt/C, (b) Ir/C, (c) Pt3Ir/C, (d) PtIr/C, (e) PtIr3/C before exposure to CO.

For the Pt_xIr_y/C group of catalysts, illustrated at Figure 5-8, it can be observed that the diffusion control region is located at potentials above ~0.08 V (vs. RHE). The mixed-control region from 0.02 to 0.08 V (vs. RHE) and the kinetic control region from 0 to 0.02 V (vs. RHE). Furthermore, it can be seen that Pt/C and Ir/C present the lowest current density at the mass transport region (almost 0.99 mA cm^{-2} and 2.76 mA cm^{-2} for 1600 rpm at ~0.08 V (vs. RHE)), where the flat plateau is observed. Respectively, for Pt_3Ir/C the limiting current density at ~0.08 V (vs. RHE) is 3 mA cm^{-2}, for PtIr/C is 3.26 mA cm^{-2} and for $PtIr_3/C$ is 3.22 mA cm^{-2} (all the prices referred to 1600 rpm).

Furthermore, from the LSV curves (Figure 5-7, 5-8, 5-9, 5-10) it is obvious that with the increase of the rotational speed of the RDE, the current density for every catalyst recorded, is also increased. The biggest limiting current density at 1600 rpm for H_2-saturated 0.1M $HClO_4$ aqueous solution, for the Pt_xPd_y/C group of catalysts is given by the $PtPd_3$/C catalyst and is 3.13 mA cm^{-2} at ~0.075 V (vs. RHE) and for the Pt_xIr_y/C group of catalysts is given by PtIr/C and is 3.26 mA cm^{-2} at ~0.08 V (vs. RHE). The wave distortion observed (Pt_xPd_y/C group of catalysts) from 0.1 to 0.2 V is probably referred to non-steady state oxidation of hydrogen dissolved in palladium as mentioned before.

Continuously, for the Figure 5-9 and Figure 5-10 all RDE experiments were conducted under H_2/N_2 10/40 (cc/min) 0.1 M $HClO_4$ aqueous solution, at a scan rate of 5 mVs-1, at rotation rates of 400 rpm, 1000 rpm, 1600 rpm, 2200 rpm, from which the corresponding linear sweep voltammetry curves (LSV) were taken. This specific ratio of gasses inserted (H_2/N_2 10/40 (cc/min)) was chosen, because this is the ratio of H_2/CO (200ppm in N_2) (10/40(cc/min)) used for investigate the CO tolerance of the tested catalysts afterwards.

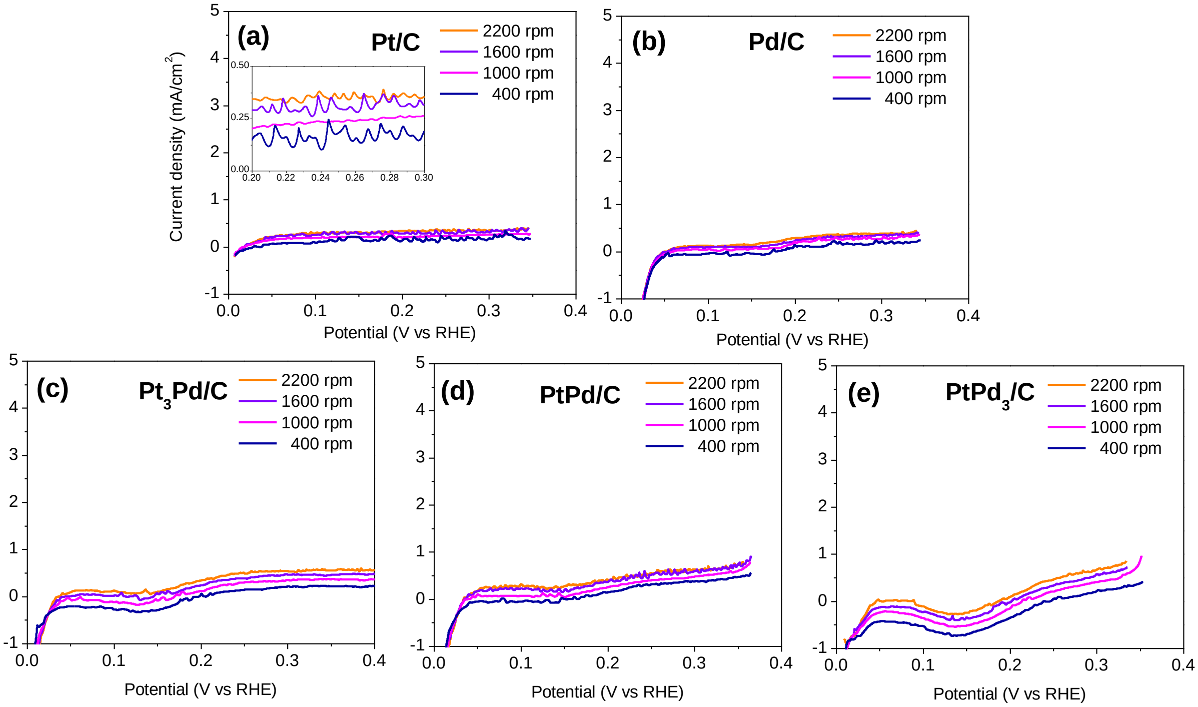

Figure 5-9 LSV curves in H2-N2 10/40 (cc/min) 0.1 M HClO4 aqueous solution, at rotation rates 400, 1000, 1600, 2200 rpm, at a scan rate of 5 mV s-1 for (a) Pt/C, (b)Pd/C, (c) Pt3Pd/C and (d) PtPd/C, (e) PtPd3/C.

For the Pt_xPd_y/C group of catalysts, illustrated at Figure 5-9, diffusion control region can be located at potentials above ~0.075 V (vs. RHE). The mixed-control region from 0.025 to 0.075 V (vs. RHE) and the kinetic control region from 0 to 0.025 V (vs. RHE). Also, as mentioned before for Figures 5-7, the wave distortion on linear sweep voltammograms, observed from 0.1 to 0.2 V at Figure 5-10, can probably be referred to non-steady state oxidation of hydrogen dissolved in palladium. As it can be seen, Pt/C and Pd/C presents the lowest current density at the mass transport region (almost 0.41 mA cm^{-2} and 1.7 mA cm^{-2} for 1600 rpm at ~0.075 V (vs. RHE)), where the flat plateau is observed. Respectively, for Pt_3Pd/C the limiting current density at ~0.075 V vs RHE is 1.89 mA cm^{-2}, for PtPd/C is 1.43 mA cm^{-2} and for $PtPd_3/C$ is 1.27 mA cm^{-2} (all the prices referred to 1600 rpm).

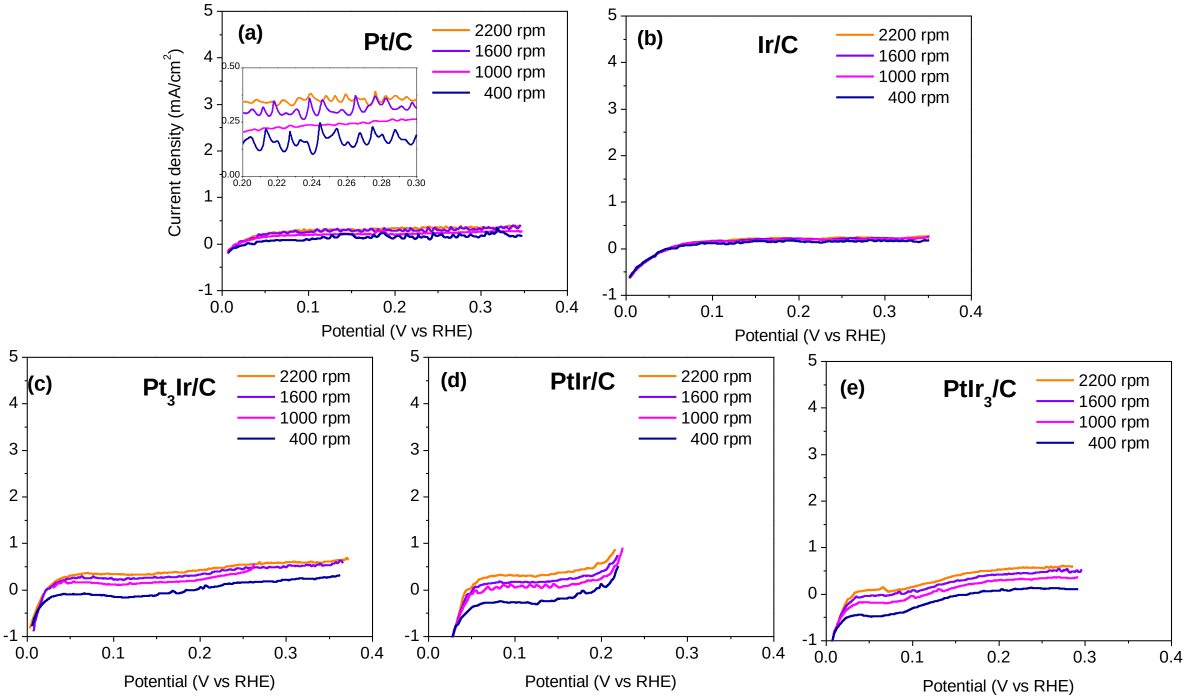

Figure 5-10 LSV curves in H_2/N_2 (10/40 cc/min) 0.1 M $HClO_4$ aqueous solution, at rotation rates 400, 1000, 1600, 2200 rpm, at a scan rate of 5 mV s^{-1} for (a) Pt/C, (b) Ir/C, (c) Pt_3Ir/C, (d) PtIr/C, (e) $PtIr_3/C$.

For the Pt_xIr_y/C group of catalysts, illustrated at Figure 5-10, diffusion control region can be located at potentials above ~0.08 V (vs. RHE). The mixed-control region from 0.02 to 0.08 V (vs. RHE) and the kinetic control region from 0 to 0.02 V (vs. RHE). Furthermore, it can be seen that Pt/C and Ir/C present the lowest current density at the mass transport region (almost 0.41 mA cm^{-2} and 0.6 mA cm^{-2} for 1600 rpm at ~0.08 V (vs. RHE)), where the flat plateau is observed. Respectively, for Pt_3Ir/C the limiting current density at ~0.08 V (vs. RHE) is 0.88 mA cm^{-2}, for PtIr/C is 3.1 mA cm^{-2} and for $PtIr_3/C$ is 1.31 mA cm^{-2} (all the prices referred to 1600 rpm).

Furthermore, from the LSV curves (Figures 5-7, 5-8, 5-9, 5-10) it is obvious that with the decrease of the fuel (H_2) inserted, the limiting current density, where the flat plateau is observed for every catalyst recorded, is also decreased. The biggest limiting current density at 1600 rpm for H_2/N_2 (10/40 cc/min) 0.1 M $HClO_4$ aqueous solution, for the Pt_xPd_y/C group of catalysts is given by the Pt_3Pd/C catalyst and is 1.89 mA cm^{-2} at ~0.075 V (vs. RHE) and for the Pt_xIr_y/C group of catalysts is given by PtIr/C and is 3.1 mA cm^{-2} at ~0.08 V (vs. RHE).

Once the rotating disk electrode treatment of the catalyst ends, the linear sweep voltammograms recorded are taken and Tafel plots are extracted. The electrocatalytic activity for the HOR can be further examined by the evaluation of the kinetic parameters derived from the analysis of the Tafel equation (5.6). These parameters are the exchange current density (i_0) and the Tafel slope at low overpotentials:

$$\log i_k = \log i_0 \left(\frac{anF}{2.303RT}\right)\eta \tag{5.6}$$

where i_k is the kinetic current, given by the equation (5.7):

$$i_k = \frac{i \times i_d}{i_d - i} \tag{5.7}$$

The kinetic current (density) is the current (density) at the given potential in the absence of mass-transport restrictions. Kinetic current (I_k) relates the reaction rate (activity) of the electrochemical reaction to a given concentration of active species. As we can see, the Table 2 presents the kinetic current, I_k (A) at different overpotential values (low 20mV, medium 100mV, and high 200mV) for 20% Pt_xPd_y/C catalysts. It can be observed, that Pt_3Pd/C catalyst performs best at low and high potential by giving the largest current, and PtPd/C performs best at medium potential.

Table 2: Kinetic current I_k when low, medium, and high potential prices are applied for catalysts Pt_xPd_y/C. Prices collected from LSV curves in H_2-saturated, 0.1 M $HCLO_4$ aqueous solution, at rotation rate of 1600 rpm, and scan rate of 5 mV s^{-1}.

Potential (mV) / Catalyst	I_k(A)				
	$PtPd_3/C$	Pt_3Pd/C	PtPd/C	Pt/C	Pd/C
20	$22.5*10^{-5}$	$30*10^{-5}$	$17.2*10^{-5}$	$8.6*10^{-5}$	$5.02*10^{-5}$
100	$65.1*10^{-5}$	$82.22*10^{-5}$	$92.2*10^{-5}$	$33.5*10^{-5}$	$11*10^{-5}$
200	$113.3*10^{-5}$	$237*10^{-5}$	$142.3*10^{-5}$	$48.9*10^{-5}$	$28.1*10^{-5}$

Respectively, the Table 3 presents the kinetic current, I_k (A) at different potential values (low 20mV, medium 100mV, and high 200mV) for 20% Pt_xIr_y/C catalysts. Pt_3Ir/C provides the highest kinetic current at low and medium potential, while at high potential Ir/C performs best.

Table 3: Kinetic current I_k when low, medium, and high potential prices are applied for catalysts Pt_xIr_y/C. Prices collected from LSV curves in H_2-saturated, 0.1 M $HCLO_4$ aqueous solution, at rotation rate of 1600 rpm, and scan rate of 5mVs-1.

Potential (mV) / Catalyst	I_k(A)				
	$PtIr_3/C$	Pt_3Ir/C	PtIr/C	Pt/C	Ir/C
20	$32.4*10^{-5}$	$63*10^{-5}$	$21.7*10^{-5}$	$8.6*10^{-5}$	$5.07*10^{-5}$
100	$146*10^{-5}$	$187.5*10^{-5}$	$128.5*10^{-5}$	$33.5*10^{-5}$	$146.6*10^{-5}$
200	$301.6*10^{-5}$	$234.7*10^{-5}$	$239.4*10^{-5}$	$48.9*10^{-5}$	$396.2*10^{-5}$

Kinetic current, also corresponds to the catalytic activity of the catalyst, and it reveals some information about the mechanism of the reaction, through calculation of the Tafel slope. The Tafel slope (mV/decade) is a measure of the catalyst activity and is calculated from the slope of the Tafel plots. The Tafel plots of the catalyst tested are presented on Figure 5-11 and Figure 5-12, below.

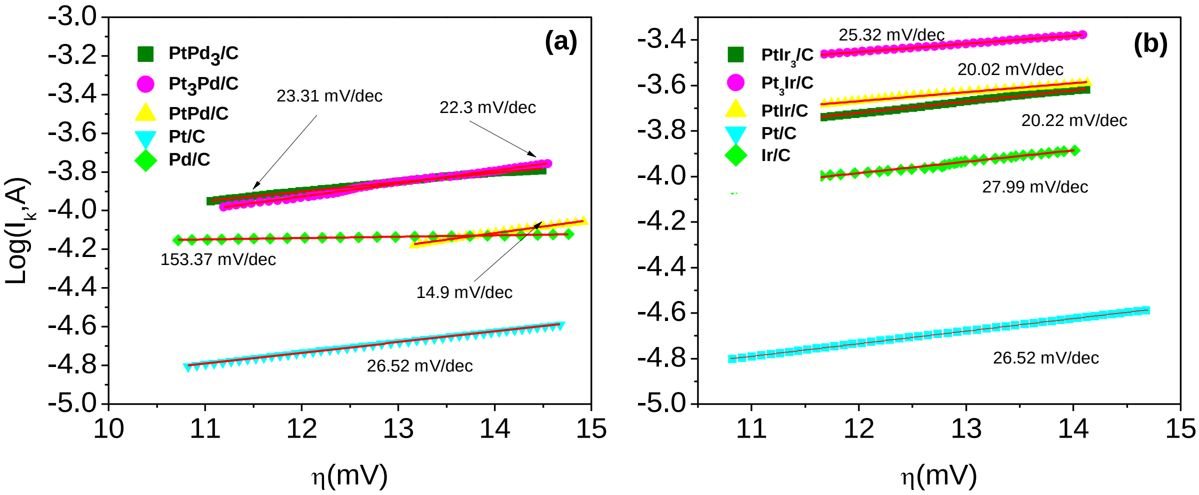

Figure 5-11 Tafel plots in H2-saturated 0.1 M HClO4 aqueous solution, at rotation rate 1600 rpm, at a scan rate of 5 mV s-1 for (a) PtxPdy/C, (b) PtxIry/C before exposure to CO.

It is known that low values of Tafel slopes are desirable, since the smaller the slope, the less the overpotential increases with the current density. Taking this into account, from Figure 5-11, it can be concluded that PtPd/C, with Tafel slope 14.9 mV/decade, has the best activity from Pt_xPd_y/C group of catalyst (Figure 5-11(a)). Pt_3Pd/C and $PtPd_3/C$ are following with 22.3 and 23.31 mV/decade. Pt/C has lower activity with Tafel slope 26.52 mV/decade and Pd/C comes last with the worst activity 153.37 mV/decade. Figure 5-11 (b) provides information about the activity of Pt_xPd_y/C group of catalysts. The best activity belong to PtIr/C and $PtIr_3/C$ follows with a small difference, Tafel slope 20.22 mV/decade. Pt_3Ir/C is ranked third with Tafel slope 25.32 mV/decade, Pt/C fourth with Tafel slope 26.52 mV/decade and Ir/C fifth with Tafel slope 27.99 mV/decade.

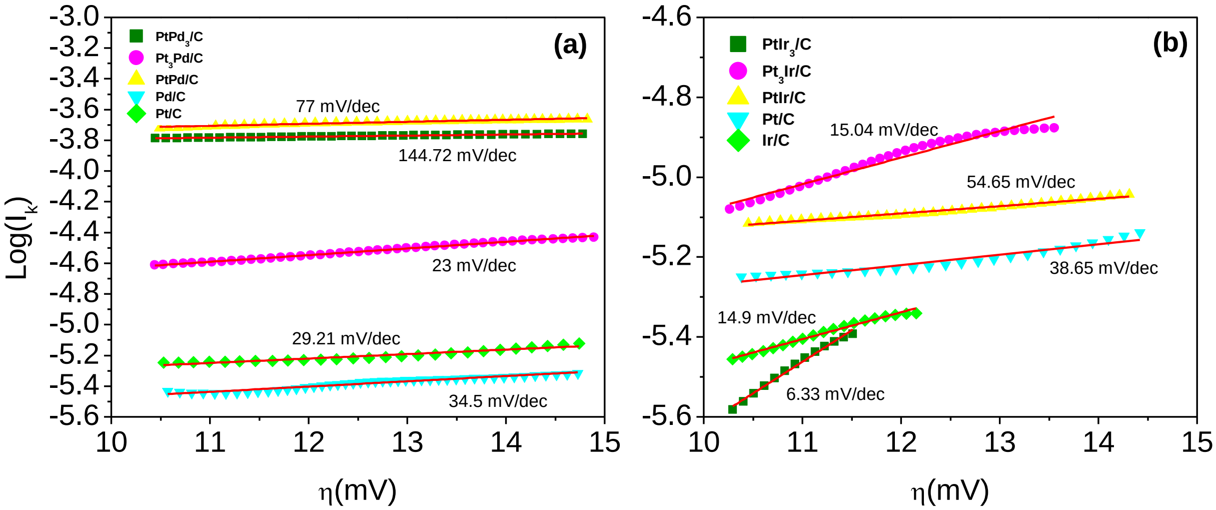

Figure 5-12 Tafel plots curves in H2/N2 (10/40 cc/min) 0.1 M HClO4 aqueous solution, at rotation rate 1600 rpm, at a scan rate of 5 mV s-1 for (a) PtxPdy/C, (b) PtxIry/C before exposure to CO.

From Figure 5-12, it can be observed that when fuel-supply drops at ratio H_2/N_2 10/40 (cc/min)), then Pt_3Pd/C with Tafel slope 23 mV/decade, has the best activity from Pt_xPd_y/C group of catalyst (Figure 5-12(a)). Pt/C is ranked second (Tafel slope 29.21 mV/decade), Pd/C third (Tafel slope 34.5 mV/decade), PtPd/C fourth (Tafel slope 77 mV/decade) and finally $PtPd_3/C$ ranked fifth with Tafel slope 144.72 mV/decade. For Pt_xIr_y/C group of catalysts (Figure 5-12(b)) $PtIr_3/C$ with Tafel slope 6.33 mV/decade has the best activity. The classification of the catalyst's activity afterwards is the following: Ir/C 14.9 mV/decade > Pt_3Ir/C 15.04 mV/decade > Pt/C 38.65 mV/decade > PtIr/C 54.65 mV/decade.

5.3.2 Investigation of electrocatalyst tolerance in the presence of carbon monoxide

Following the experimental measurements, the effect of time on CO tolerance of electrocatalysts was studied. More specifically, the adsorption rate of CO for 3, 6 and 9 hours of exposure to 400ppm CO in hydrogen flow at -0,2V (vs. RHE), of the electrocatalysts under investigation.

5.3.2.1 Chronoamperometry results

To compare the CO tolerance of the 20 w.t.% Pt_xPd_y/C catalysts with the 20 w.t.% Pt_xIr_y/C catalysts, chronoamperometry was used to evaluate the performance of the catalysts in the presence of 400 ppm CO in fuel gas (Figure 5-13).The potential was fixed at -0.2 V, and the performance of the catalysts was studied for time intervals of 3, 6, and 9 hours. During the first 5-10 minutes, pure H_2 was supplied as gas until stabilization of the current density was achieved, after the 5-10 minutes, pure H_2 was superseded by a mixture of H_2 and 400 ppm CO for 3, 6 ,9 hours test of CO tolerance of both catalyst series. From the results of the chronoamperometry the Pt_xPd_y/C series showed better CO tolerance than that showed by Pt_xIr_y/C catalyst series as can be seen in Figure 5-13.

Based on the results of chronoamperometry for the single-metal Ir/C, Pt/C and Pd/C catalyst there is a sharp decline at the first 30 minutes of the measurement, which indicates the catalyst poisoning by CO, thus these catalysts show minimum to none tolerance towards CO.

It can be observed that in the cases of Pt/C, Pd/C and Ir/C electro-catalysts under investigation their life expectancy under the test conditions could not succeed the 1.5 hour, 2 and 1 hours respectively**.** But with the composition of bimetallic catalyst, Pt_xIr_y/C and Pt_xPd_y/C in different atomic ratios, it was able to overcome the barrier of 2 hours of current density to reach zero [41].

For the bimetallic catalysts and more specifically for the Pt_xIr_y/C catalyst it can be concluded that the PtIr/C catalyst demonstrated the worst tolerance in presence of 400 ppm CO, with the current density dropped to zero after only 1.5 hours of the experiment. $PtIr_3/C$ catalyst showed a moderate tolerance towards CO with the current dropped almost zero after 4.5 hours. From the bimetallic Pt_xIr_y/C catalyst series the one with superior tolerance to CO was Pt_3Ir/C with the current having a gradual decline from 3 hours until its final fall to zero at 6 hours. The bimetallic Pt_xPd_y/C catalyst, all three of them showed greater tolerance to CO than Pt_xIr_y/C catalysts. This can be observed from the fact that they endured for the time interval of 9 hours in presence of 400 ppm CO. As a first stage for the emergence of the catalyst with the highest tolerance towards CO, the current densities at the end of the chronoamperometries (9 hours) can be compared. It is obvious that $PtPd_3/C$ exhibits the higher tolerance, with a current density of 0.17 mA cm^{-2}, second in the series being Pt_3Pd/C with 0.11 mA cm^{-2} and third being PtPd/C with 0.02 mA cm^{-2}.

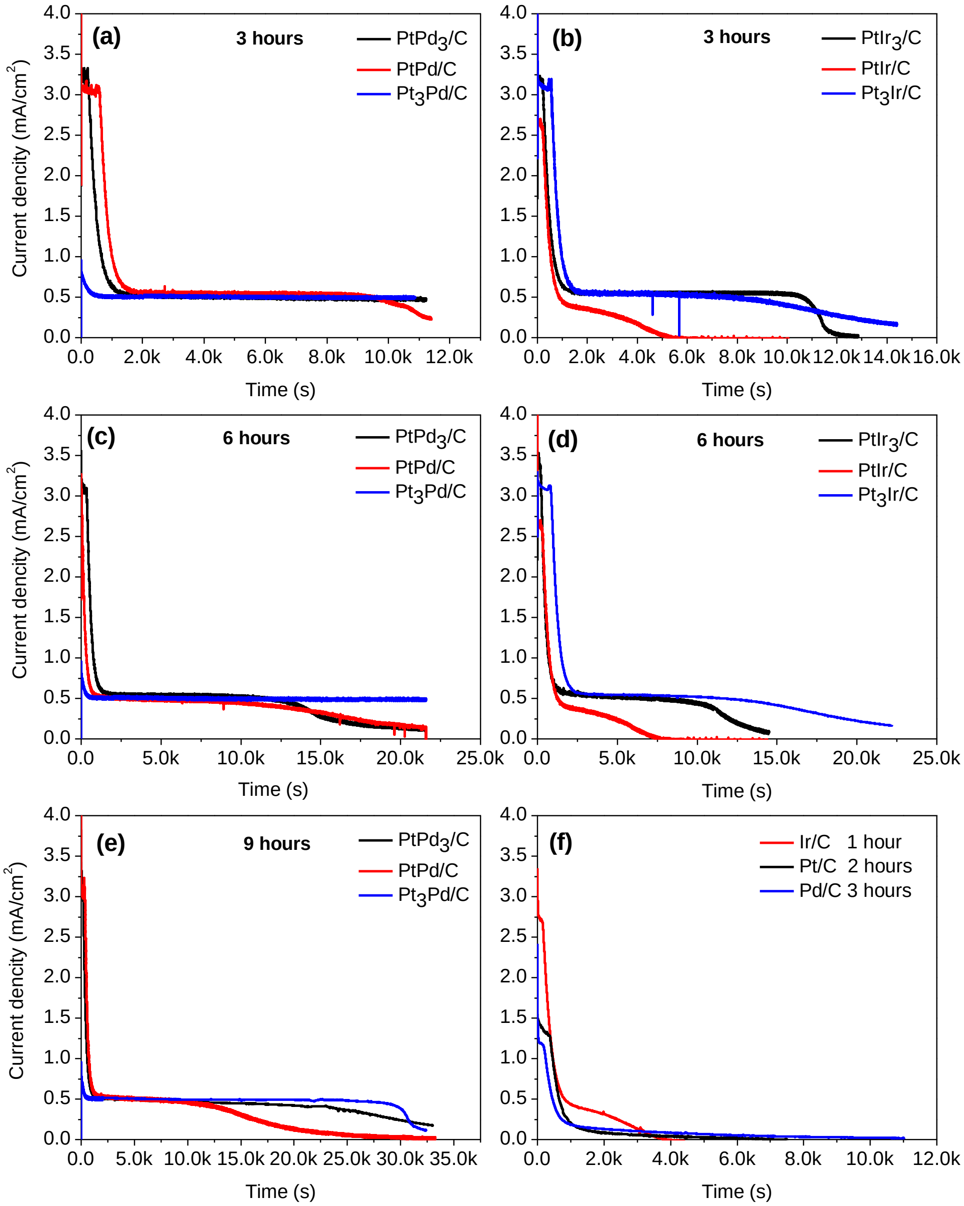

Figure 5-13 Chronoamperometry results: curves of (a) Pt_xPd_y/C duration 3 hours, (b) Pt_xIr_y/C duration 3 hours, (c) Pt_xPd_y/C duration 6 hours, (d) Pt_xIr_y/C duration 6 hours, (e) Pt_xPd_y/C duration 9 hours, (f) Ir/C, Pt/C and Pd/C electrocatalyst for the durations 1, 2, 3 hours respectively in H_2/CO 10/40 (cc/min) 0.1 M $HCLO_4$ aqueous solution at 1600 rpm, at -0,2V potential step.

The biggest drop of current density in all measurements at the first 5-10 minutes is due to the change of fuel from pure hydrogen at 50cc min^{-1} to a mixture of H_2/CO with flow rate of 10/40cc min^{-1}. This change of the fuel caused a shortage of dissolved hydrogen in the electrolyte, thus less hydrogen oxidation that leads to less electrons released to the system and subsequently lower current density. When the system reaches “steady state” conditions it is observed that for the duration of the chronoamperometry there is a small decline of the current density over time in all catalysts. This is firstly due to weariness of the catalysts and it can be observed even when the fuel during this procedure is pure hydrogen. Secondly when the fuel contains even a small amount of carbon monoxide this decline is much greater than the one on pure hydrogen, this is due to the adsorption of CO. This results in catalyst active surface being covered by CO. As a consequence, less and less catalyst active centers are available for adsorption and desorption of hydrogen which leads to the drop of current density over time and resulting current density to reaching zero. The CO coverage depends on the exposure time and the ppm of CO on the fuel.

The fact that the decline of current density was delayed and with the results of cyclic voltammetry after chronoamperometry which show the magnitude of the poisoning from CO means that the bimetallic catalyst has a much greater tolerance to CO. For more precise results where the true extent of the poisoning due to carbon monoxide is evident, the following section is set out below.

The rate of CO adsorption on the electrochemically active surface is calculated by the following equation [42]:

$$\theta_{CO} = \frac{S_{CO}}{S} \tag{5.6}$$

where, S_{CO}: the electrochemically active surface occupied by the adsorbed CO

S: the hydrogen adsorption surface

The surface occupied by adsorbed CO on the electrochemically active surface is calculated by the following equation [42]:

$$S_{CO} = \frac{Q_{CO}}{0.420\ \mathrm{mC\ cm^{-2}}} \tag{5.7}$$

where, Q_{CO} is the charge (mC) of adsorbed carbon monoxide. The adsorbed carbon charge is calculated by integration of the graphed area of curve 1 from Figure 5-14. Integration does not include the area occupied by area (2) (green dashed area), 0.420 mC cm^{-2} the charge corresponding to a layer of adsorbed carbon monoxide [42].

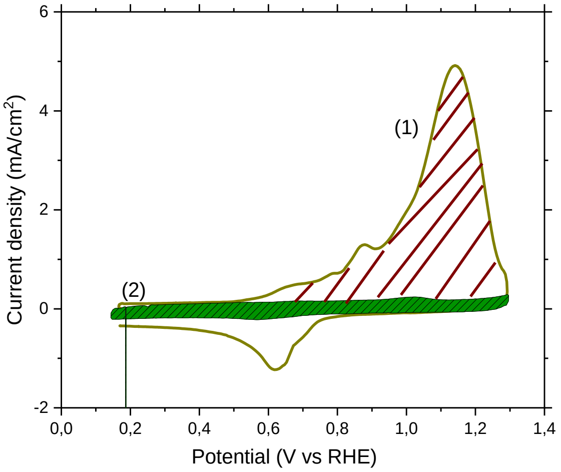

Figure 5-14 Electrooxidation of adsorbed CO in 0.1M $HClO_4$, 50 mV s^{-1}**.**

More specifically, the Figure 5-14 shows the 1st cycle of cyclic voltammogram after the complete CO oxidation. The measurement of cyclic voltammetry took place after the exposure of the electrocatalyst, for the time intervals under investigation, to a specific potential and CO concentration, with the usage of chronoamperometry.

The electro-oxidation of the adsorbed CO (area 1, Figure 5-14) is achieved via cyclic voltammetry. It is observed that the adsorbed CO is fully oxidized from the first cycle, as shown by the area 2 of Figure 5-14 with no electro-oxidation peak.

The hydrogen adsorption surface prior to exposure to CO calculated by the following equation [42]:

$$S = \frac{Q_H}{\theta_H \times 0.210 mCcm^{-2}} \qquad (5.8)$$

where, Q_H : the charge of an adsorbed atomic hydrogen single layer.

θ_H : the coverage rate at the highest potential (0.77) [43].

5.3.2.2 *Effect of time on CO tolerance of electrocatalysts*

The results of electrooxidation of adsorbed carbon monoxide for Pt_xPd_y/C catalysts at different exposure times are shown in Figure 5-15.

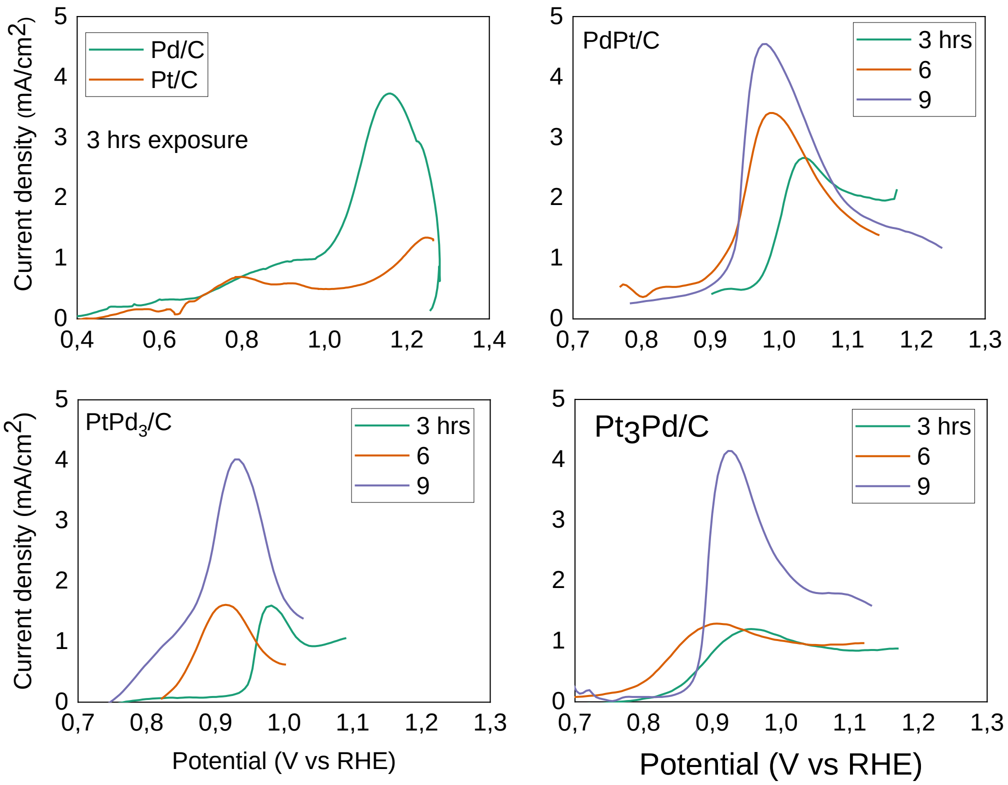

Figure 5-15 Electrooxidation of adsorbed carbon monoxide in 0.1M $HClO_4$, 50mV s^{-1}.

Based on the Figure 5-15, the onset potential of electrooxidation of carbon monoxide appear to shifts to lower potential values with the increase of time exposure. Also, the peak potential of electrooxidation is lower in case of 6 hours exposure. In more detail, the values of the electrooxidation potential and the CO electrooxidation peak potential are listed in Table 4.

Table 4: CO electrooxidation information.

Hours of exposure	Peak CO electrooxidation (V vs RHE)					Onset potential CO electrooxidation (V vs RHE)				
	PdPt/C	PtPd$_3$/C	Pt$_3$Pd/C	Pd/C	Pt/C	PdPt/C	PtPd$_3$/C	Pt$_3$Pd/C	Pd/C	Pt/C
3	0,98	0,98	0,96	1,15	0,8	0,96	0,92	0,79	0,67	0,64
6	0,99	0,92	0,9	-	-	0,87	0,83	0,77	-	-
9	1,0	0,93	0,93	-	-	0,87	0,75	0,85	-	-

Among the catalysts under investigation, $PtPd_3$/C exhibits the highest tolerance at the presence of CO at all exposure times (Figure 5-16 (a)). PtPd/C exhibits the lowest tolerance at the presence of carbon monoxide with carbon monoxide covering 40% of the electrochemically active surface after nine hours of exposure time. Next comes Pt_3Pd/C with almost 27% coverage of active centers, followed by $PtPd_3$/C with 25% coverage. The same rank is also followed for the three and six-hours exposure at 400ppm CO.

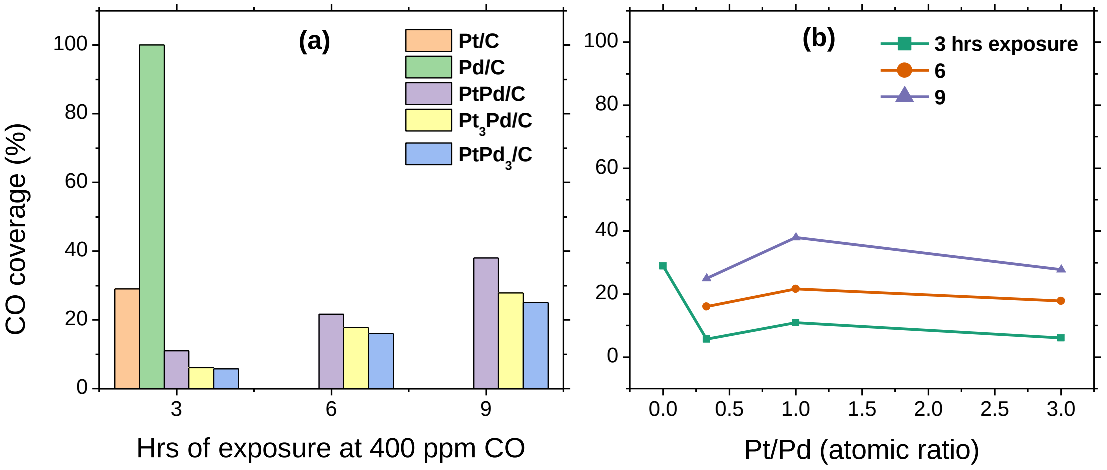

Figure 5-16 Percentage coverage of active centers with CO, as a function of exposure time at 400 ppm CO (a), percentage of coverage of active centers by CO as a function of Pt / Pd ratio (b).

From Figure 5-16 (a) it is also observed for all catalysts that as the exposure time at CO increases the CO coverage (poisoning) rate at the catalyst increases linearly. Finally, Figure 5-16 (b) shows a volcano-type correlation between the Pt / Pd ratio and the CO coverage rate.

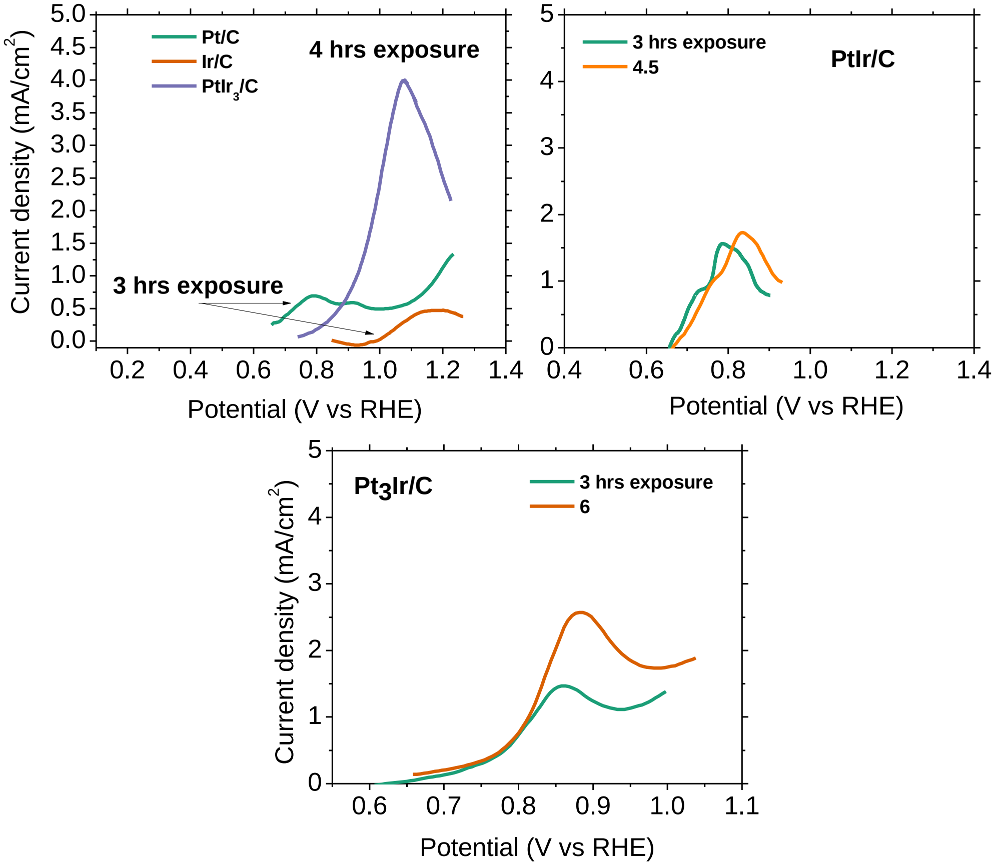

Figure 5-17 Electrooxidation peaks of CO for Pt$_x$Ir$_x$/C catalysts

On the basis of the correlation, it appears that the presence of palladium over a certain amount helps to lower the catalyst poisoning by CO.

Following the experiments, the tolerance of the Pt_xIr_y/C bimetallic electrocatalysts in the presence of carbon monoxide is investigated. As it can be observed from Figure 5-17, it is characteristic that $PtIr_3/C$ was 100% poisoned in the first three hours indicating the sensitivity of Ir to the presence of carbon monoxide. The electrocatalyst which exhibited the highest tolerance at 3 and 6 hours of CO exposure is Pt_3Ir / C.

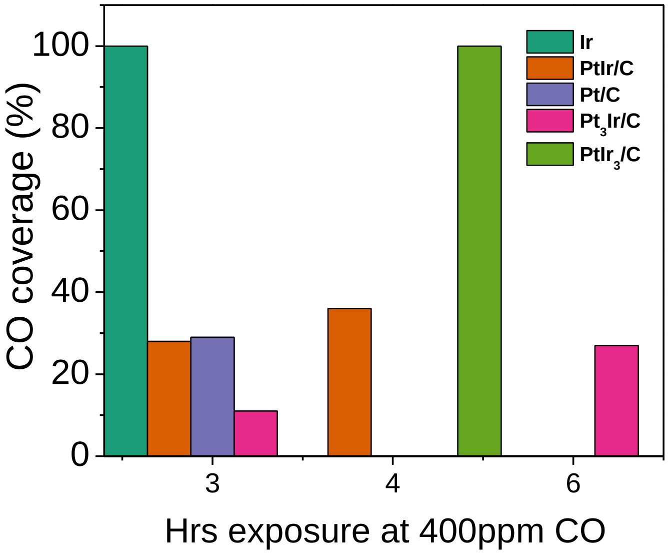

Figure 5-18 Percentage coverage of active centers with CO, as a function of exposure time at 400 ppm CO for Pt_xIr_y/C group of electrocatalysts.

More specifically, as shown in Figure 5-18 at 3 hours of exposure the surface coverage rate was 10% and at 6 hours exposure almost 30%. The PtIr/C catalyst shows 28% of CO coverage at 3 hours of exposure and 40% at 4.5 hours of exposure. This shows that the PtIr/c exhibits a higher tolerance than that of $PtIr_3/C$ but less tolerance than Pt_3Ir/C. From these results it is possible to conclude that with higher atomic ratios of Ir in the catalyst the tolerance to CO decreases.

Generally, Ir/C presents a good activity for the HOR at PEMFCs, but certainly lower than Pt/C. Ir particles have the tension to aggregate, reducing not only the catalyst surface area, but also the hydrogen oxidation reaction area[44].

Subsequently Figure 5-19 shows the linear scanning curves before exposure to CO and after exposure for 3, 6, and 9 hours, respectively and the corresponding Tafel curves, extracted as mentioned before (chapter 4.3.2) with the Tafel slopes calculated for each curve separately.

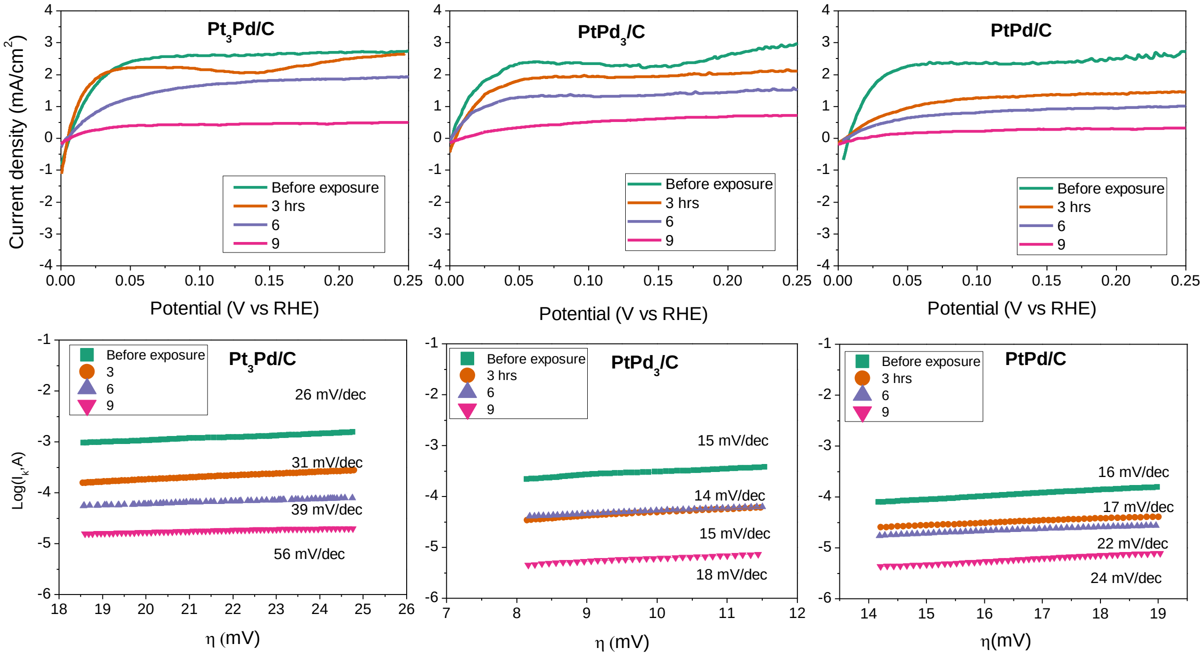

Figure 5-19 Linear scan curves in H2-saturated 0.1M HClO$_4$, 1600 rpm, before exposure to CO and after exposure for 3,6 and 9 hours (top line) and Tafel curves for the corresponding linear scan curves.

It is observed for all three catalysts that as the exposure time to CO increases, the slope also increases. This is interpreted by the fact that the longer the exposure time, the greater the rate of poisoning of the catalyst, which requires higher overpotential rates to be applied for hydrogen electrooxidation. Based on the Tafel slope values the catalytic activity drops while the exposure time to CO increased. The decrease of the catalytic activity, with the increase of the time exposure, indicates the magnitude of CO poisoning. Based on the decrease of the catalytic activity the order of poisoning is: Pt$_3$Pd/C> PtPd/C> PtPd$_3$/C. Tafel's results are also in agree with the results of calculating coverage rates.

CHAPTER VI

6 Concluding remarks

In this section, after all the experimental results evaluated to estimate which of the tested catalyst has the best behavior. First, for HOR, by checking their ECSA, their activity and the current they produce when specific voltages applied. Second, for CO-poisoning, by the calculation of CO-coverage on the catalyst's surface. Results from other papers on the same topic of Hydrogen Oxidation Reaction and CO-tolerance for various catalysts in PEMFCs-H_2, are also included, in order to have the opportunity to discuss and compare with our own experimental values. This comparison can provide us an assessment on the efficiency and the tolerance of our electrocatalysts.

Table 5: Main peak potentials ($E_{main\ peak}$) and relative ratios of catalyst sites poisoned by CO for a series of Pt_xPd_y catalysts tested at 25° C [45].

Catalysts Tested / T(°C)	$E_{mainpeak}$(V)	θ_{CO}
	25°C	25°C
Pt	0.718	1
PtPd	0.775	0.99
$PtPd_2$	0.777	0.96
$PtPd_4$	0.811	0.96
$PtPd_6$	0.816	0.93
Pd	0.852	0.95

Table 5, shows CO oxidation potentials and CO-coverage, calculated form cyclic voltammograms of different Pt_xPd_y catalysts at 25°C, in 0.5 M H_2SO_4, at a scan rate of 5 mV s^{-1}. For 25°C, only a small part of Pt_xPd_y surface remains non-poisoned after CO saturation. In the same study the effect of the temperature is tested. With the increase of temperature at 80°C a slight decrease of the CO-coverage is observed. In this case, the surface of the Pt particles for Pt/C remains fully blocked by CO, but as long as the metal loading of Pd increased, a decrease in CO-

coverage is observed, with CO cover the 73% of the adsorbed hydrogen area on Pd/C [45]. A similar behavior observed on carbon-supported PdAu electrocatalysts [46].

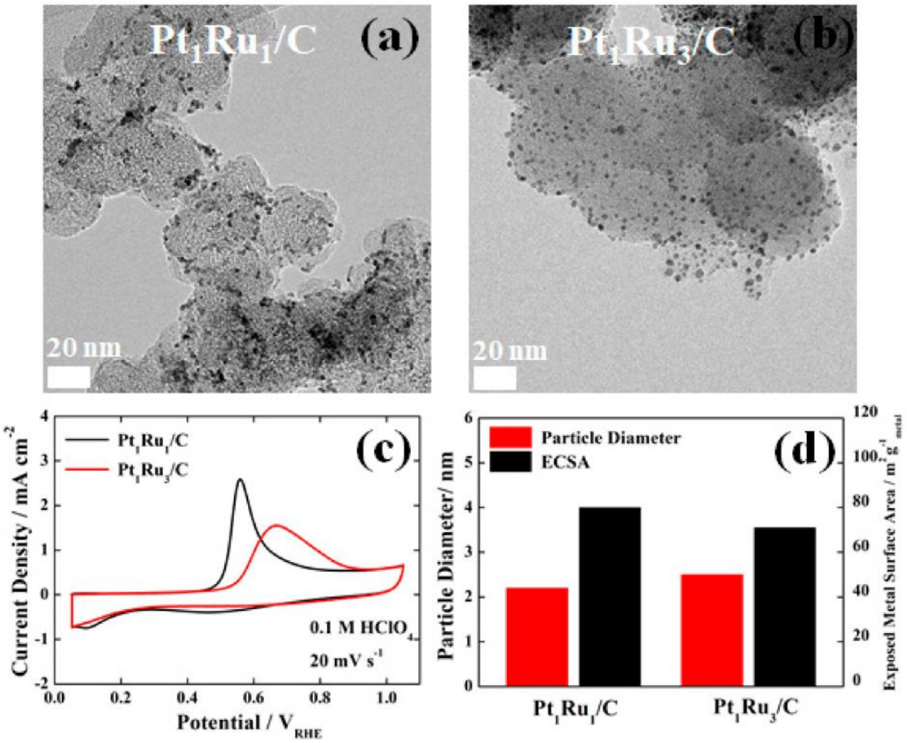

Figure 6-1 Transmission electron microscopy images (TEM) of (a) PtRu/C and (b) $PtRu_3/C$, (c) CO-stripping curves and (d) particle diameters and ECSAs of PtRu/C and $PtRu_3/C$ [41].

As shown in Figure 6-1, PtRu/C and $PtRu_3/C$ has similar enough particle diameters that were estimated from the TEM images in Figure 6-1 (a), and (b). In this paper, researchers use the CO-stripping curves in order to estimate the ECSA values. From the above results, they concluded that PtRu/C and $PtRu_3/C$ catalysts have a similar particle size and similar surface area as well, while they have different CO-binding energies due to different Ru content. To investigate the CO-tolerance of the catalysts, the evaluation technique that conducted, was chronoamperometry. Definitely, the results show that a Pt/C catalyst without Ru indicated much lower CO tolerance in the chronoamperometry tests.

The results as it is obvious, confirm that for Pt_xM_y catalysts, when the metal loading start to increase, the CO-tolerance also increased. Of course, for some specific ratios, there is better behavior [41].

In this work, the HOR electrocatalytic activity and CO tolerance of Pt, Ir, Pd, Pt_xPd_y, Pt_xIr_y on Vulcan XC-72 (20 w.t. % metal loading, atomic ratios 3:1, 1:1 and 1:3) electrocatalysts were examined. From the cyclic voltammetry experimental measurements for the w.t. 20% anode catalysts (Pt_xIr_y/C, Pt_xPd_y/C) of PEMFCs at 30 ^{0}C in 0.1 M $HClO_4$ aqueous solution, from 0.1V and 1.2V (vs. RHE), scan rate 50 mV sec^{-1} it was concluded, that the highest electrochemical active surface area for the Pt_xIr_y/C catalyst was for Pt_3Ir/C and for the Pt_xPd_y/C catalyst was for $PtPd_3/C$ with 32.39 and 123.07 m^2 g$^{-1}_{metal}$ respectively, as shown in Table 1.

The HOR activity of the tested electrocatalysts was examined by rotating disk electrode (RDE) experiments, from which the corresponding linear sweep voltammetry curves (LSV) were taken (Figure 5-7 and 5-8), in H_2-saturated 0.1 M $HClO_4$ aqueous solution, at 1600 rpm with 5 mV s^{-1} scan rate. As it can be seen for the Pt_xPd_y/C catalysts, the highest limiting current density (presented at mass transport region ~0.075 V (vs. RHE)) was given by $PtPd_3/C$ 3.13 mA cm^{-2}, second comes PtPd/C with 2.86 mA cm^{-2} and Pt_3Pd/C follows with 2.65 mA cm^{-2}. Furthermore, for the Pt_xIr_y/C catalysts the order from highest to lowest limiting current density (presented at mass transport region ~0.08 V (vs. RHE)) is: PtIr/C (3.26 mA cm^{-2}), $PtIr_3/C$ (3.22 mA cm^{-2}) and Pt_3Ir/C (3 mA cm^{-2}). The single-metal catalysts (Pt/C, Ir/C and Pd/C) have lower limiting current densities than the bimetallic catalysts tested.

Additionally, from the LSV curves the Tafel plots were extracted.

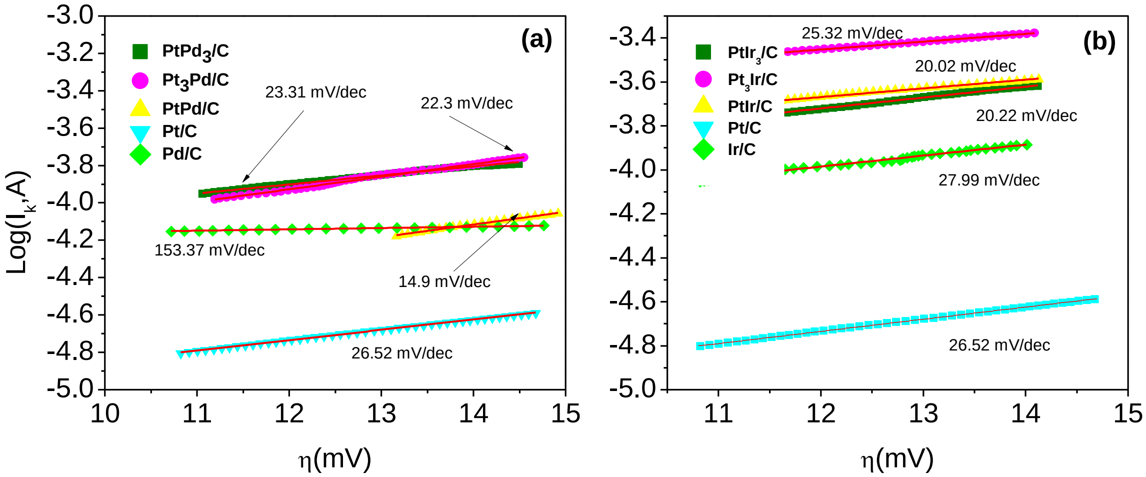

Figure 6-2 Tafel plots in H_2-saturated 0.1 M $HClO_4$ aqueous solution, at rotation rate 1600 rpm, at a scan rate of 5 mV s^{-1} for (a) Pt_xPd_y/C, (b) Pt_xIr_y/C before exposure to CO.

Low values of Tafel slopes are desirable, since the smaller the slope, the less the overpotential increases with the current density. The Tafel slopes values inform us about the activity of the catalyst. Taking this into account, from Figure 6-2 (a), a classification of the activity of Pt_xPd_y/C group of catalysts results: PtPd/C 14.9 mV/decade > Pt_3Pd/C 22.3

mV/decade > $PtPd_3$/C 23.31 mV/decade > Pt/C 26.52 mV/decade > Pd/C 153.37 mV/decade. Figure 6-2 (b) provides information about the activity of Pt_xPd_y/C group of catalysts respectively. The order results as: PtIr/C 20.2 mV/decade > $PtIr_3$/C 20.22 mV/decade > Pt_3Ir/C 25.32 mV/decade > Pt/C 26.52 mV/decade > Ir/C 27.99 mV/decade.

Afterwards, the chronoamperometry experiments were conducted for different time intervals 3, 6, 9 hours, with potential step -0.2 V (vs. RHE). From the chronoamperometry results it was observed that the Pt_xPd_y/C where superior to Pt_xIr_y/C regarding the test conditions with PtPd/C, $PtPd_3$/C and Pt_3Pd able to withstand for 9 hours, where respectively PtIr/C and $PtIr_3$/C last for 4 hours with the exception of Pt_3Ir/C which lasted for 6 hours. The figure below (Figure 6-3 (a), (b)) presents the maximum chronoamperometry duration of each catalyst.

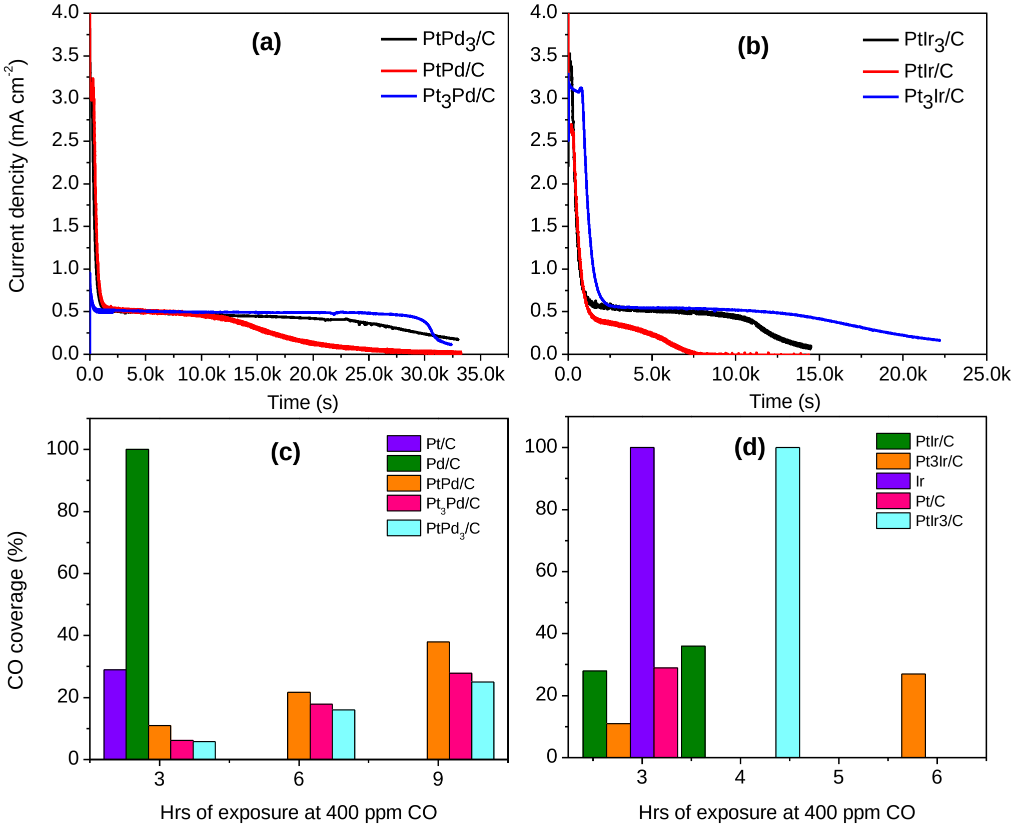

Figure 6-3 (a)Pt_xPd_y/C, (b) Pt_xIr_y/C maximum hours of chronoamperometry in H_2/CO 10/40 (cc/min) 0.1 M $HClO_4$ aqueous solution at 1600 rpm, at -0,2V potential step. Percentage coverage of active centers with CO, as a function of exposure time at 400 ppm CO for (c) Pt_xPd_y/C and (d)Pt_xIr_y/C.

From the CO stripping that followed after the CO poisoning of the catalysts it is obvious that the Pt_xPd_y/C catalyst shown higher tolerance in presence of CO with the superior catalyst being $PtPd_3$/C with 25% carbon monoxide coverage in presence of 400 ppm CO after

9 hours of time exposure. For the Pt_xIr_y/C group of catalysts the higher tolerance to CO was shown by Pt_3Ir/C catalysts with almost 30% coverage after 6 hours of exposure, as shown in the figure above (Figure 6-3 (c), (d)).

The Pt_xPd_y/C group of catalysts were more CO tolerant than Pt_xIr_y/C, following the measurements conducted after the chronoamperometry. This is why further measurements were carried out for this specific group (Pt_xPd_y/C). Linear sweep voltammograms and Tafel plots extracted after chronoamperometry, are presented below to show the drop in current density and the catalyst activity in relationship with the exposure time to CO (Figure 6-4).

From the LSV measurements (Figure 6-4 (a), (c), (e), (g)) is obvious that current density significantly drops after the exposure to CO. This is due to the fact that catalyst active centers are blocked by the adsorbed CO. It is obvious that the single-metal catalysts show no tolerance towards CO with the current density dropping almost to zero. The best behavior exhibited by the $PtPd_3/C$ catalyst with the current density being 0.5 mA cm^{-2} after 9 hours of exposure followed by Pt_3Pd/C with 0.3 mA cm^{-2} and PtPd/C with 0.1 mA cm^{-2} for the same time of exposure.

From the figure below (Figure 6-4 (b), (d), (f), (h)) it is obvious that by combining Pt and Pd at different atomic ratios, the Tafel slope can be reduced even after the catalyst being poisoned for different time intervals. More specifically after 9 hours of exposure, the $PtPd_3/C$ catalyst exhibits the smallest slope, among all Pt_xPd_y/C catalysts. This means that this catalyst is more active towards HOR at low overpotentials, with a slope of 18 mV dec^{-1} after 9 hours of exposure to CO and only 3 mV dec^{-1} rise of its Tafel slope compared with the Tafel plots before exposure to CO, when for Pt_3Pd/C the rise is 30 mV dec^{-1} and for PtPd/C is 40 mV dec^{-1} for the same time of exposure.

To sum up, by the physicochemical characterizations, such as X-ray diffraction (XRD), scanning electron microscopy (SEM) and transmission electron microscopy (TEM) and the electrochemical characterizations by cyclic voltammetry, electrochemical impedance spectroscopy, linear sweep voltammetry (using RDE) and chronoamperometry we made some remarks for the activity and the CO-tolerance of the tested catalysts. With experiments in real fuel cells and fuel cells stacks can be determined the suitability of the catalysts for real time operation. This study it is not yet fully integrated and further experiments must be conducted inside a working fuel cell in order to obtain a complete view of the catalysts.

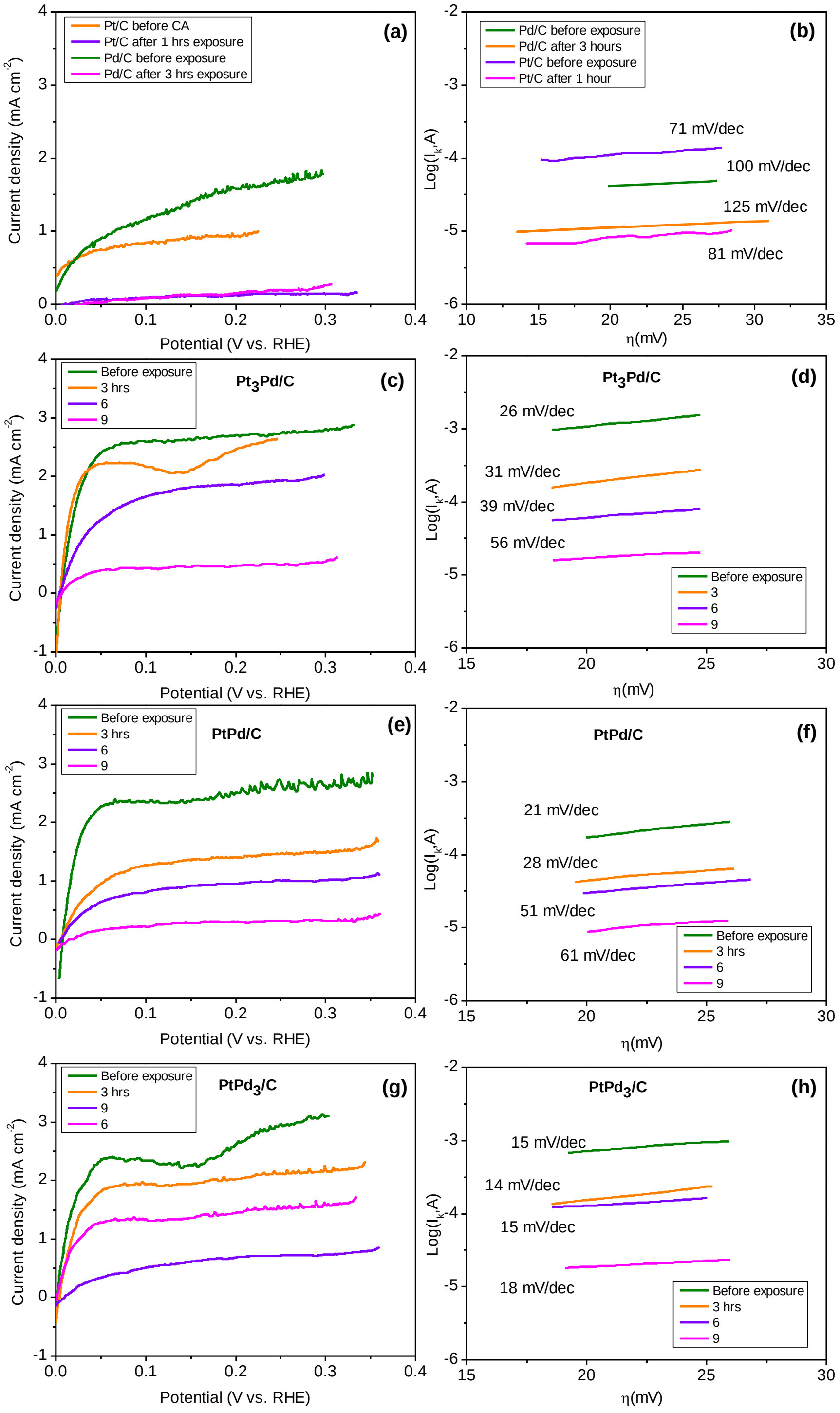

Figure 6-4 LSV curves (a, c, e, g) and the corresponding Tafel plots(b, d, f, h) in H_2-saturated 0.1 M $HClO_4$ aqueous solution, at 1600 rpm, at a scan rate of 5 mV s^{-1} for Pt_xPd_y/C catalysts before and after exposure to CO for different time intervals.

Parameters like the effect of temperature and water flooding must be considered before reaching a full verdict. An extra factor that must be taken into account and effects the selection of the electrocatalyst for the HOR is the cost of the noble metals used for catalysts. Commonly, Platinum was the most expensive metal among those who presented high HOR activity. Nowadays, Palladium and Iridium prices have skyrocketed, making them less favorable materials for electrocatalysts. Nevertheless, the fuel cells improvements and their contribution on reducing carbon emission intensity, including the progress on hydrogen's way of production and storage, will soon led to fully commercialization of fuel cells.

7 References

[1] H.D. Yoo, E. Markevich, G. Salitra, D. Sharon, D. Aurbach, Materials Today 17 (2014) 110-121.
[2] https://www.worldenergydata.org/world/#footnote_4_2840, in.
[3] O. Ellabban, H. Abu-Rub, F. Blaabjerg, Renewable and Sustainable Energy Reviews 39 (2014) 748-764.
[4] https://learnmechanical.com/hydroelectric-power-plant/, in.
[5] A. Godula-Jopek, D. Stolten, Hydrogen Production: by Electrolysis, Wiley, 2015.
[6] https://www.elprocus.com/batteries-types-working/, in.
[7] W.R.W. Daud, R.E. Rosli, E.H. Majlan, S.A.A. Hamid, R. Mohamed, T. Husaini, Renewable Energy 113 (2017) 620-638.
[8] P.D. Richards, R.J. Myers, S.M. Swinton, R.T. Walker, Global Environmental Change 22 (2012) 454-462.
[9] https://www.powerelectronictips.com/fundamentals-supercapacitor-balancing/, in.
[10] J. Zhang, L. Zhang, H. Liu, A. Sun, R.S. Liu, Electrochemical Technologies for Energy Storage and Conversion, 2 Volume Set, Wiley, 2011.
[11] Y. Wang, K.S. Chen, J. Mishler, S.C. Cho, X.C. Adroher, Applied Energy 88 (2011) 981-1007.
[12] J. Zhang, PEM Fuel Cell Electrocatalysts and Catalyst Layers: Fundamentals and Applications, Springer London, 2008.
[13] W. Sheng, H. Gasteiger, Y. Shao-Horn, Journal of The Electrochemical Society 157 (2010) B1529.
[14] O.T. Holton, J.W. Stevenson, Platinum Metals Review 57 (2013) 259-271.
[15] F.T. Wagner, B. Lakshmanan, M.F. Mathias, The Journal of Physical Chemistry Letters 1 (2010) 2204-2219.
[16] A. Abaspour, N. Tadrisi Parsa, M. Sadeghi, International Journal of Computer Applications 97 (2014) 25.
[17] Q. Li, R. He, J.-A. Gao, J.O. Jensen, N.J. Bjerrum, Journal of The Electrochemical Society 150 (2003) A1599.
[18] X. Cheng, Z. Shi, N. Glass, L. Zhang, J. Zhang, D. Song, Z.-S. Liu, H. Wang, J. Shen, Journal of Power Sources 165 (2007) 739-756.
[19] Chapter 10 Catalyst characterization with spectroscopic techniques, in: J.A. Moulijn, P.W.N.M. van Leeuwen, R.A. van Santen (Eds.), Studies in Surface Science and Catalysis, vol 79, Elsevier, 1993, pp. 363-400.
[20] A. Morlang, U. Neuhausen, K.V. Klementiev, F.W. Schütze, G. Miehe, H. Fuess, E.S. Lox, Applied Catalysis B: Environmental 60 (2005) 191-199.
[21] S.L. Flegler, J.W. Heckman, K.L. Klomparens, Scanning and Transmission Electron Microscopy: An Introduction, Oxford University Press, 1993.
[22] https://en.wikipedia.org/wiki/Transmission_electron_microscopy, in.

[23] W.D. Pyrz, D.J. Buttrey, Langmuir 24 (2008) 11350-11360.

[24] W. Zhou, Z.L. Wang, Scanning Microscopy for Nanotechnology: Techniques and Applications, Springer New York, 2007.

[25] A. Ul-Hamid, A Beginners' Guide to Scanning Electron Microscopy, Springer International Publishing, 2018.

[26] W. Xing, G. Yin, J. Zhang, Rotating Electrode Methods and Oxygen Reduction Electrocatalysts, Elsevier Science, 2014.

[27] C.G. Zoski, Handbook of Electrochemistry, Elsevier Science, 2007.

[28] N. Elgrishi, K.J. Rountree, B.D. McCarthy, E.S. Rountree, T.T. Eisenhart, J.L. Dempsey, Journal of Chemical Education 95 (2018) 197-206.

[29] P.T. Kissinger, W.R. Heineman, Journal of Chemical Education 60 (1983) 702.

[30] D. Barrow, A. Patil, A. Rinzler, (2004).

[31] L. Peng, S.-J. You, J.-Y. Wang, Biosensors & bioelectronics 25 (2010) 2530-2533.

[32] https://chem.libretexts.org/, in.

[33] https://www.tissuegroup.chem.vt.edu/chem-ed/echem/linsweep.html, in.

[34] https://www.palmsens.com/electrochemical-impedance-spectroscopy-eis/, in.

[35] P. Kissinger, W.R. Heineman, Laboratory Techniques in Electroanalytical Chemistry, Second Edition, Revised and Expanded, Taylor & Francis, 1996.

[36] L. Wang, Q. Han, S. Hu, D. Li, P. Zhang, S. Chen, J. Xu, B. Liu, Applied Catalysis B: Environmental 164 (2015) 128-134.

[37] S.J. Hwang, S.J. Yoo, T.-Y. Jeon, K.-S. Lee, T.-H. Lim, Y.-E. Sung, S.-K. Kim, Chemical Communications 46 (2010) 8401-8403.

[38] A. Allagui, M. Oudah, X. Tuaev, S. Ntais, F. Almomani, E.A. Baranova, International Journal of Hydrogen Energy 38 (2013) 2455-2463.

[39] T. Lopes, E. Antolini, E.R. Gonzalez, International Journal of Hydrogen Energy 33 (2008) 5563-5570.

[40] Electrochemical Water Splitting: Materials and Applications, Materials Research Forum LLC, 2019.

[41] J. Min, A.A. Jeffery, Y. Kim, N. Jung, Nanomaterials 9 (2019) 1425.

[42] T. Vidaković, M. Christov, K. Sundmacher, Electrochimica Acta 52 (2007) 5606-5613.

[43] quot, S. Chatrchyan, quot, quot, V. Khachatryan, quot, quot, A.M. Sirunyan, quot, quot, C.T. CMS, T. Collaborations, quot, quot, a. others, quot, European Physical Journal. C Medium: X; Size: page(s) 1-26.

[44] E. Antolini, ChemElectroChem 1 (2014) 318-328.

[45] F.J. Rodríguez-Varela, T.W. Napporn, Advanced Electrocatalysts for Low-Temperature Fuel Cells, Springer International Publishing, 2018.

[46] H. Wang, H. Li, X.Z. Yuan, PEM Fuel Cell Failure Mode Analysis, CRC Press, 2011.